



**HAL**  
open science

## Validation of the hydrodynamics in a turbulent un-baffled stirred tank: A necessity for vortex-reactor precipitation studies

E. Saikali, M.G. Rodio, G. Bois, U. Bieder, N. Leterrier, M. Bertrand, Y. Dolias

### ► To cite this version:

E. Saikali, M.G. Rodio, G. Bois, U. Bieder, N. Leterrier, et al.. Validation of the hydrodynamics in a turbulent un-baffled stirred tank: A necessity for vortex-reactor precipitation studies. *Chemical Engineering Science*, 2020, 214, pp.115426. 10.1016/j.ces.2019.115426 . cea-02526170

**HAL Id: cea-02526170**

**<https://cea.hal.science/cea-02526170>**

Submitted on 7 Mar 2022

**HAL** is a multi-disciplinary open access archive for the deposit and dissemination of scientific research documents, whether they are published or not. The documents may come from teaching and research institutions in France or abroad, or from public or private research centers.

L'archive ouverte pluridisciplinaire **HAL**, est destinée au dépôt et à la diffusion de documents scientifiques de niveau recherche, publiés ou non, émanant des établissements d'enseignement et de recherche français ou étrangers, des laboratoires publics ou privés.



Distributed under a Creative Commons Attribution - NonCommercial 4.0 International License

# Validation of the hydrodynamics in a turbulent un-baffled stirred tank: a necessity for vortex-reactor precipitation studies

E. Saikali<sup>1,\*</sup>, M.G. Rodio<sup>1</sup>, G. Bois<sup>1</sup>, U. Bieder<sup>1</sup>, N. Leterrier<sup>1</sup>, M. Bertrand<sup>2</sup> and Y. Dolias<sup>3</sup>

<sup>1</sup> DEN – Service de Thermo-hydraulique et de Mécanique des Fluides (STMF), CEA, Université Paris-Saclay, 91191 Gif-sur-Yvette, France,

<sup>2</sup> DEN – Département de Recherche sur les Procédés pour la Mine et le Recyclage du Combustible (DMRC), CEA, 30207 Bagnols-sur-Cèze, France,

<sup>3</sup> DRT – Direction des Partenariats Industriels (DPI), CEA, 38000 Grenoble, France,

\*[elie.saikali@cea.fr](mailto:elie.saikali@cea.fr)

---

## Abstract

This paper is devoted to large eddy simulations of a turbulent flow in an un-baffled stirred tank reactor with vortex effect. The work aims at providing reference solutions regarding the hydrodynamics and the different mixing regions. Such data serve in modelling the precipitation process that takes place in many chemical engineering applications. The numerical study is performed by the open source TrioCFD code that employs a discontinuous front-tracking algorithm to solve the free surface at the top of the reactor. A sufficiently converged mesh has been identified from a sensitivity analysis where a convergence at the same order of the employed numerical scheme has been recorded. The quality of the resolved fields confirm that the performed LES is good and that the mesh size is almost of the Taylor turbulent micro-scale order. The converged statistical fields have shown a good agreement with both the theoretical models and the experimental measurements.

**Keywords:** Reactor with vortex effect (RVE); Large Eddy Simulation (LES); Wall-adapting local eddy-viscosity (WALE); Chemical reactors; TrioCFD; Mesh sensitivity.

---

## 1. Introduction

Precipitation is an important topic that takes place in a wide range of energy related procedures as battery recycling and radioactive waste processing. Such chemical reactions are well known to be very fast and can lead to the formation of solid particles. As a safety assessment, whether for the manipulation or the transport of the product, it is critical to understand correctly the physical/chemical properties of the formed particles and is thus classified as one of the main research themes at the Atomic Energy Commission and alternative energies (CEA) in France.

As detailed in [1], mixing tank reactors with an industrial design are often considered in studies to avoid waste manipulation at large scales. Baffled reactors are widely used in experimental and/or numerical studies [2, 3, 4]. In such a configuration, obstacles are introduced into the test vessel in order to break the circular motion generated by the mixer. This results in a dominant vertical fluid motion with an efficient turbulent macro-mixing. However, attrition and accumulation zones can build up in the reactor due to the canceling of the fluid rotational movement. This situation reduces the efficiency of the process and can lead to a major issue such as the blocking of the impeller. For this reason, and since the nuclear industries try to avoid accumulation zones as much as possible to facilitate the maintenance procedures, an un-baffled tank is modelled in the present study. Here, the fluid is agitated by a magnetic rod that rotates at the bottom of the reactor without the presence of obstacles [5].

According to the work of [6] and based on the mathematical Rankine's combined vortex model [7], the rotational movement of the rod creates a vortex at the free surface. This results in a flow that can be characterized by two macro-mixing zones. A first zone situated at the center of the reactor, described by a vertically-downwardly oriented vortex and referred to as the "forced vortex". In this region, the fluid rotates as a solid body with an angular velocity not far from that of the rod. The second mixing zone is that between the vertical walls and the forced vortex. It is characterized by a helicoid trajectory with an upward orientation and referred to by the free vortex. Owing this behavior, such type of a reactor is cited as a reactor with a vortex effect (RVE). Figure 1 illustrates the presence of these vortices from a numerical simulation obtained by [8]. To our knowledge, studies devoted to RVE's are scarcely documented in the literature.

Precipitation reactions are known to be highly influenced by the presence of the two zones of vortices and thus the reactor can not be assumed as well-mixed. For that, a hydrodynamic model is necessary used to identify the complex flow pattern and to simulate the precipitation process. Computational fluid dynamics (CFD) approaches have proven efficient in predicting the local/global flow behavior when such an observation is difficult experimentally. In this paper, the numerical approach is followed. However, the most challenging point is the choice of a good turbulence model since performing direct numerical simulations (DNS) for industrial applications is too expensive and/or almost impossible.

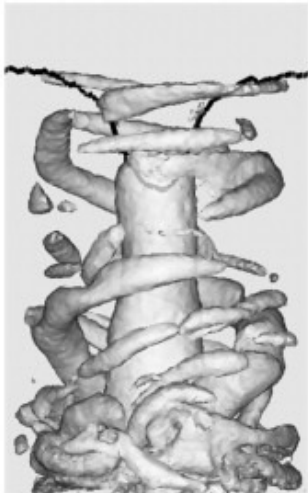


Figure 1: 3D iso-surfaces of the Q-criterion from [8] illustrating the forced and the free vortices present in the reactor.

The circular rotation of the magnetic rod makes the tangential velocity component dominant and thus builds a strong anisotropic turbulence in the domain. This is a weak point for linear Reynolds-Averaged Navier-Stokes (RANS) models and thus limits their use [9, 10]. Large Eddy Simulations (LES) approaches, which are based on spatially filtered Navier-Stokes equations, have been shown to be a good alternative tool to RANS and satisfactorily results in similar types of flows are recorded [11, 12]. Moreover, both instantaneous and fluctuating fields are accessed with LES, in addition to the ability of capturing the macro-instabilities that are important for the mixing study. Reynolds-stress models and non-linear RANS models might also be a good candidates for this study. However, in order not to enlarge the present work, the focus was set on LES. The filtering of the LES considered here is implicitly introduced by the mesh. This is equivalent to saying that length scales larger than the characteristic size of the mesh are solved. Length scales smaller than the mesh size are modelled by an appropriate sub-grid scale (SGS) model [13].

Some results had been presented in [8] where the authors illustrated the ability of the LES in reproducing the flow pattern. Comparisons versus experimental Laser Doppler Velocimetry (LDV) measurements of the CEA and the theoretical work of [6] have shown a satisfactorily agreement. Moreover, they explained in [14] how the CFD predictions can be employed afterwards in the population balance (PB) models to identify and describe the formation of the solid particles that form at the bottom of the reactor due to the oxalic precipitation.

The objective of this work is to present reference LES data of the considered problem with a thorough validation. More precisely, the aim is to provide satisfactorily converged numerical predictions regarding the hydrodynamics and the mixing zones in the reactor, independently of the employed mesh. For that, the grid sensitivity and the LES quality are thoroughly analyzed. There are two main reasons behind why this study has been performed. Firstly, providing such a reference numerical data is extremely important and interesting as far as it can

serve as a tool of validation in future works. Secondly, accurate LES predictions should provide a correct hydraulics basis for an accurate knowledge of the precipitation process and on the shape/size of the solid particles that form. The document is organized as follows. In section two, the model is set and the LES equations are presented. The numerical setup and the computational tools are discussed in section three. Section four is devoted to the mesh sensitivity analysis. Here, a sufficiently converged mesh is identified. The instantaneous and time-averaged flow patterns are presented in section five. Validations versus LDV and theoretical models are the subject of section six. Conclusions and perspectives are drawn finally in section seven.

## 2. Physical and numerical model

### 2.1. Configuration

The geometry of the RVE modelled here is the one introduced by [5] and described as a cylinder of height  $H$  and diameter  $T$  ( $H/T \approx 1.6$ ). As shown in figure 2, the cylinder is open at the top and filled with water at rest to a height  $H_i < H$ . At the bottom-center, a magnetic rod of length  $D$  ( $D/T \approx 0.47$ ) and diameter  $d$  ( $D/d \approx 6.7$ ) is placed. The rod rotates in the clockwise direction with a constant rotational frequency  $N$  and is thus responsible of the fluid movements in the domain. The stirring Reynolds number is  $Re_s = ND^2/\nu \approx 7 \times 10^4$  and thus the flow is completely turbulent [15]. Assuming a room temperature, the properties of the working fluids are presented in table 1. The interfacial surface tension coefficient  $\sigma$  is considered uniform and constant;  $\sigma = 0.07 \text{ N.m}^{-1}$ .

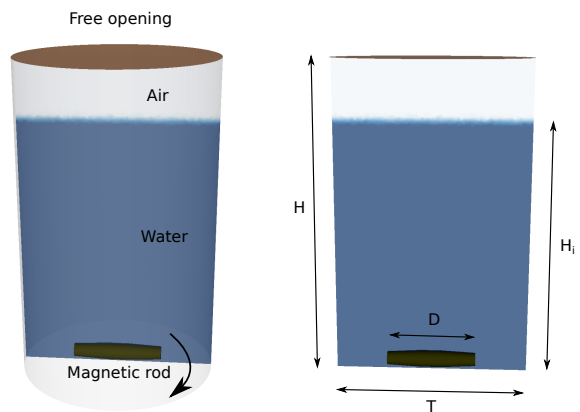


Figure 2: Schematic representation of the RVE geometry with both 3D and 2D views.

Fluid	Density [ $\text{kg.m}^{-3}$ ]	Kinematic viscosity [ $\text{m}^2.\text{s}^{-1}$ ]
Water	$\rho_w = 1000$	$\nu_w = 1 \times 10^{-6}$
Air	$\rho_a = 1.29$	$\nu_a = 2 \times 10^{-5}$

Table 1: Physical properties of the working fluids at room temperature.

## 2.2. Governing equations

The flow in the RVE is governed by the conservation equations of mass and momentum. Due to the iso-thermal condition and supposing that there is no phase-change phenomenon, solving an additional equation for energy conservation is not required here.

Assuming no density variations in each fluid and since a low Mach number flow is considered, the fluid is assumed incompressible. For simplicity, the governing equations are presented in this subsection as for a case of a single-fluid, which is exact and holds true far from the free surface laying between the liquid/gas fluids. However, the complete formulation of two-phase flows is taken into account in the numerical calculations and the surface tension, density and viscosity jumps are considered at the interface. The reader is kindly invited to refer to [16, 17] for the complete two-phase fluid formulation with surface tension and different properties in each phase.

The filtered LES equations read

$$\nabla \cdot \bar{\mathbf{u}} = 0, \quad (1)$$

$$\frac{\partial \bar{\mathbf{u}}}{\partial t} + (\bar{\mathbf{u}} \cdot \nabla) \bar{\mathbf{u}} = -\frac{1}{\rho} \nabla \bar{P} + \nu \Delta \bar{\mathbf{u}} - \nabla \cdot \bar{\boldsymbol{\tau}}^{\text{SGS}} + \bar{\mathbf{F}}, \quad (2)$$

where  $\{ \bar{\cdot} \}$  denotes the spatial filtering operation for the resolved scales, while  $\{\nabla, \nabla \cdot, \Delta\}$  denote the gradient, divergence and Laplacian operators respectively. The velocity vector is  $\mathbf{u} = (u_1, u_2, u_3)$ ,  $\rho$  is the density,  $P$  the pressure and  $\nu$  the kinematic viscosity.  $\mathbf{F}$  denotes the sum of the external forces, say the gravitational force  $\mathbf{g} = (0, 0, -9.81)$  for example.

$\bar{\boldsymbol{\tau}}^{\text{SGS}}$  denotes the SGS-stress tensor that appears from applying the filtering operation on the Navier-Stokes equation. It is defined in terms of the tensorial product operation  $\otimes$  as

$$\bar{\boldsymbol{\tau}}^{\text{SGS}} = \overline{\mathbf{u} \otimes \mathbf{u}} - \bar{\mathbf{u}} \otimes \bar{\mathbf{u}}. \quad (3)$$

With length scales smaller than the characteristic grid size, the term  $\bar{\boldsymbol{\tau}}^{\text{SGS}}$  is not solved and thus equation (2) is not closed. To close the system, the Reynolds-stress tensor should be modelled so that its effect is taken into account. In this paper, the wall-adapting local eddy-viscosity (WALE) model is employed [18]. This model is based on an eddy-viscosity assumption and is known to perform better than the classical model of Smagorinsky [19] especially near the solid boundaries, in shear layers and laminar-turbulent transitional phases. The SGS viscosity is therefore calculated as

$$\nu^{\text{SGS}} = (C_W \Delta)^2 \frac{(S^d : S^d)^{3/2}}{(S^d : S^d)^{5/4} + (\bar{S} : \bar{S})^{5/2}}, \quad (4)$$

where  $C_W = 1/2$  is the constant parameter of the WALE model.  $\{ : \}$  is the tensorial contraction operator and  $\Delta$  is the characteristic grid (filter) size taken as the cubic root of the cell volume.  $S^d$  is defined in terms of the symmetrical part of the mean strain tensor  $\bar{S}$  and its rotational part  $\bar{\Omega}$  as

$$S^d = \bar{S}^2 + \bar{\Omega}^2 - \frac{1}{3}(\bar{S} : \bar{S} + \bar{\Omega} : \bar{\Omega})\mathbb{I}. \quad (5)$$

For simplicity, the overbar symbol  $\{ \bar{\cdot} \}$  is removed in the following text, keeping in mind that all fields presented in the results correspond to the solved (filtered) ones.

## 3. Setup and computational tools

### 3.1. CFD software and numerical methods

The numerical simulations are performed by the CEA open source TrioCFD software [20, 21]. Since a two-phase flow is considered, the physical properties of each fluid are independently used (table 1). However, the same velocity and pressure fields are considered for both phases. A Discontinuous Front Tracking (DFT) method is employed to capture the free surface formed between the two fluid phases. In the DFT algorithm, the free surface is defined as moving connected-marker points (Lagrangian grid), independent from the employed Eulerian mesh [22]. As described in [23], the markers of the moving grid are advected by the velocity field which is interpolated from the solution to Navier-Stokes equations computed on the Eulerian mesh. The new marker's positions are used to update the phase indicator function, and thus the physical properties of each phase; density and viscosity.

To model the effect of the magnetic stirrer on the fluid, the Immersed Boundary Method (IBM) with a Direct Forcing (DF) approach is used [24]. An independent Lagrangian mesh is defined for this boundary, which rotates with a constant speed defined as that desired for the rod. The low computational cost is a main advantage of the DF method as the forcing term is independent of the flow history. The effect of the moving boundary on the fluid is applied on the fixed Cartesian nodes of the Eulerian mesh in the vicinity of the fluid-solid interface [25]. Practically, the effect is added as an additional penalization source term to the momentum equation (2) and treated finally in the fixed reference frame of the reactor.

The spatial discretization is handled by a Finite Element Volume (VEF) discretization of second order [26]. Time marching is explicitly treated and the Courant-Friedrichs-Lewy (CFL) criterion is respected to ensure the stability of the numerical scheme. It is important to emphasize that the stability criterion of the convective term is dominant over the diffusive one in this problem. The velocity-pressure coupling is treated by a projection method satisfying equation (1) at the end of each time step. A conjugate gradient (CG) method with symmetrical-successive over relaxation (SSOR) preconditioning is used finally to solve the elliptic pressure Poisson equation.

### 3.2. Meshing

From the previous calculation [8], the maximal velocity values and the significant gradients are situated in the vicinity of the agitator and in the forced vortex formed at the central region of the tank. Thus, the mesh in these regions has been refined more than that of the neighboring free vortex zone. The volume of the reactor has been decomposed into four zones as illustrated in figure 3. The first two zones are at the bottom and in the center respectively where a fine mesh is required. The third zone is defined near the walls where a fine mesh is also considered to improve the accuracy in the near wall flow. Finally, the fourth region is nothing but the remaining part of the tank where a coarser mesh can be employed.

In order to perform a sensitivity analysis with sufficiently converged mesh, six different unstructured tetrahedral meshes

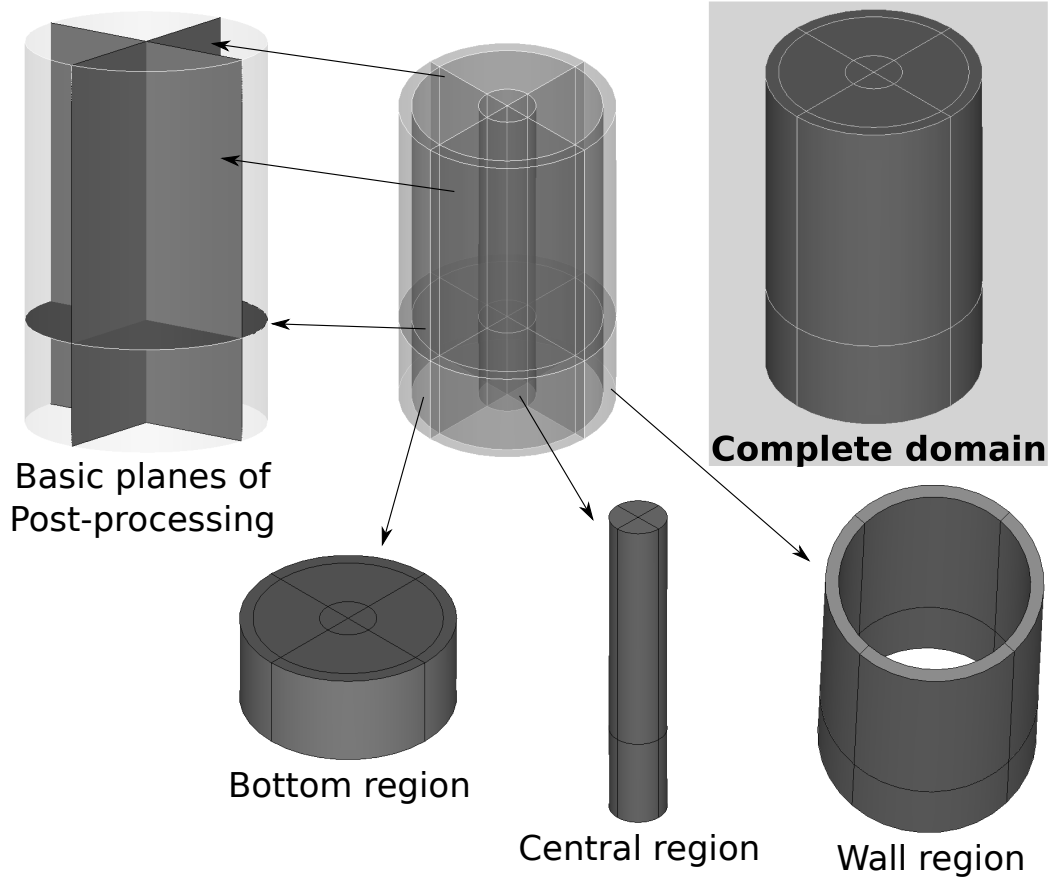


Figure 3: Schematic representation of the RVE geometry illustrating the decomposition used to generate a mesh with different spatial resolution.

have been generated, thanks to the SALOME platform [27]. The six meshes are referred to respectively as Mesh 1, 2 to 6. Mesh 1 is the coarsest mesh while the finest is Mesh 6 and thus considered as the reference. The overall mesh-quality (cells aspect ratios) is similar in all cases and a homogeneous cell distribution is satisfactorily achieved. An example of the mesh quality is described for Mesh 5 in figure. Table 2 summarizes the six mesh characteristics and the performed calculations. Here,  $\Delta$  and  $\delta$  denote respectively the maximum and the minimum size of the cell .

### 3.3. Initial and boundary conditions

In the previous work of [8], the fluid in the RVE was assumed initially at rest ( $\mathbf{u} = 0$ ) with a flat free-surface profile. With such an initial state, it had been figured that the flow attains a quasi-steady solution with a well developed flow after at least 90 complete rotations of the rod. In order to reduce the computational time to achieve a well established flow, the initial state of the RVE is considered in the present study as follows. The velocity field is initialized as that obtained with the previous coarse LES of [8]. Here, TrioCFD adapts the field by interpolating/extrapolating to the employed mesh, ensuring a divergence free condition of equation (1).

The free surface is prescribed at the initial state by a Nagata reference profile. Its height  $h$  is defined as a function of the

radial direction  $r$  as follows

$$\begin{cases} h(r) = h_v + \frac{1}{2}D \pi^2 \left(\frac{2r_c}{D}\right)^2 \text{Fr} \left(\frac{r_c}{r}\right)^2 & : r \leq r_c, \\ h(r) = h_v + \frac{1}{2}D \pi^2 \left(\frac{2r_c}{D}\right)^2 \text{Fr} \left[2 - \left(\frac{r_c}{r}\right)^2\right] & : r > r_c, \end{cases} \quad (6)$$

where  $h_v$  is the height of the vortex tip,  $r_c$  is the critical radius defined as the radial position of the forced/free vortices boundary and  $\text{Fr} = N^2 D/g$  is the dimensionless Froude number. Figure 5 shows the initial state of the RVE with the Nagata free-surface vortex and the velocity vector field.

On the wall boundaries situated at the sides and the bottom of the cylinder, a no-slip condition is defined. A standard wall-law of Richardson [13] is employed to model the boundary layer not resolved by the mesh. At the top opening, a free open boundary with a fixed pressure is considered. The contact angle of the free surface with the lateral solid boundary is fixed all the time to  $90^\circ$ . Similar to what has been observed in the experiment, a rotational law is prescribed for the magnetic rod so that its center of gravity follows the trajectory described in figure 6.

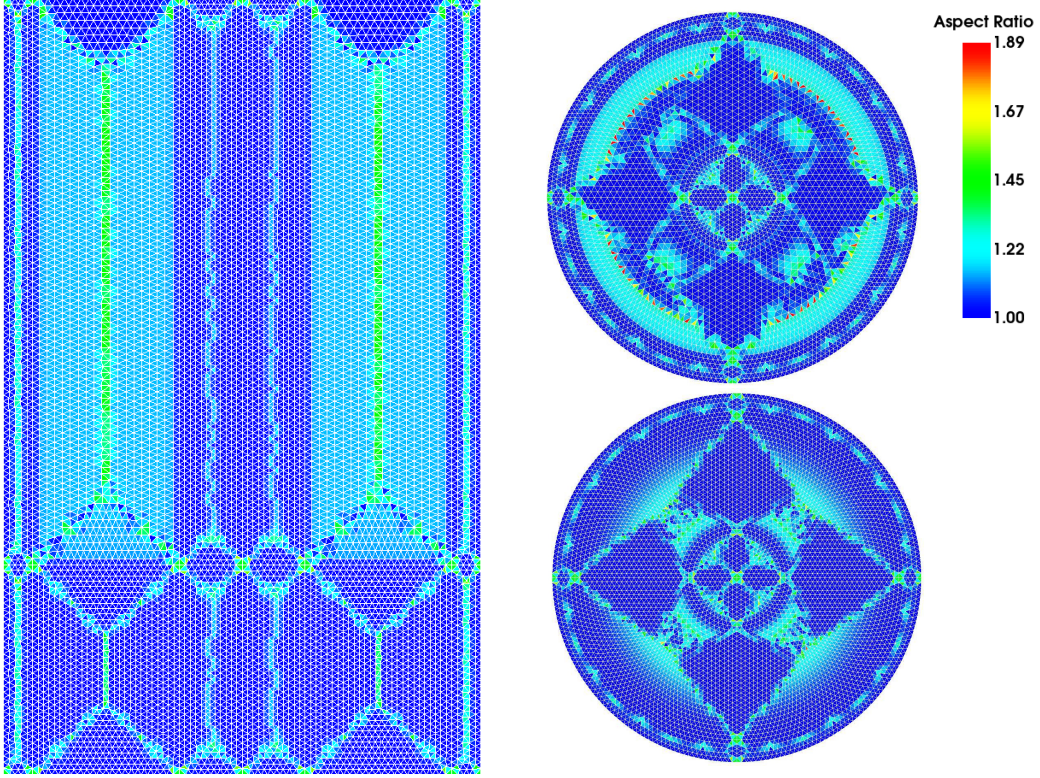


Figure 4: Aspect ratio illustrating the quality of Mesh 5. Left: 2D mid-vertical  $xz$ -plane, right-top: top open boundary, right-bottom: bottom wall boundary.

Mesh Name	Mesh 1	Mesh 2	Mesh 3	Mesh 4	Mesh 5	Mesh 6
$T/\Delta$	29	33	38	46	57	76
$T/\delta$	33	38	46	57	76	114
Aspect ratio	1 – 1.74	1 – 1.78	1 – 1.85	1 – 1.86	1 – 1.89	1 – 1.92
Cells number	352,450	524,503	841,976	1,581,629	3,354,943	9,506,418
MPI procs	28	28	28	56	112	364
Computational cost [ days ]	3.5	7.6	14	18	27.4	16
Average $\delta t^*$ [ $\times 10^{-3}$ ]	1.2	1	0.8	0.6	0.4	0.2
Maximum $t^*$	177	177	177	177	177	76

Table 2: Description of the six meshes and LES configurations.

### 3.4. Dimensionless parameters, quasi-steadiness and statistical recordings

Numerical results presented in this document are without dimensions. They are denoted by \* upper-script and calculated as follows.

- Velocity related variables are normalized as  $u_i^* = u_i/\mathbf{u}_r$ , where  $\mathbf{u}_r = \dot{\theta}D/2 = \pi ND$  is the reference velocity of the stirrer.
- Space related dimensionless variables are defined as  $r^* = 2r/T$  along the radial direction,  $\theta^* = \theta/2\pi$  along the angular direction and  $z^* = z/H$  along the vertical direction.
- The dimensionless time is considered as  $t^* = Nt$ . This value corresponds to the total number of complete rotations performed during the calculation.

The numerical calculations have been carried out on the OCCIGEN super-calculator of CINES (recall table 2 for the simulations summary) [28]. In all cases, a quasi-steady state solution has been well established at  $t^* = 20 - 25$  (to be compared with  $t^* = 85 - 90$  if the RVE is at rest in its initial state). The time averaged and the root mean square (RMS) fields are defined for a considered quantity  $\varphi(\mathbf{x}, t)$  respectively as

$$\langle \varphi(\mathbf{x}, t) \rangle_t = \frac{1}{t_{\text{end}} - t_{\text{start}}} \int_{t_{\text{start}}}^{t_{\text{end}}} \varphi(\mathbf{x}, t) dt, \quad (7)$$

$$\text{RMS}\{\varphi(\mathbf{x}, t)\}_t = \left( \frac{1}{t_{\text{end}} - t_{\text{start}}} \int_{t_{\text{start}}}^{t_{\text{end}}} (\varphi'(\mathbf{x}, t))^2 dt \right)^{1/2}. \quad (8)$$

$\varphi'$  denotes here the fluctuating part of  $\varphi$ , centered on the mean value, and defined as  $\varphi'(\mathbf{x}, t) = \varphi(\mathbf{x}, t) - \langle \varphi(\mathbf{x}, t) \rangle_t$ .



Figure 5: Nagata free-surface vortex and velocity vector field illustrating the initial state of the RVE.

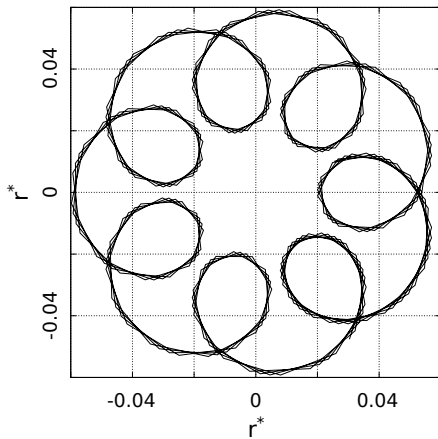


Figure 6: The trajectory followed by the rods center of gravity during the rotational movement at the bottom of the reactor according to the prescribed law.

denotes the starting time of the statistical recordings, while  $t_{\text{end}}$  corresponds to the end of the accumulation. The value of  $t_{\text{start}}$  is precised later depending on the study.

#### 4. Sensitivity of the mesh on the quality of the calculation

##### 4.1. Qualitative influence

First a qualitative comparison is discussed regarding the influence of the mesh on the quality of the captured free surface. In the DFT method, the free surface is defined by a Lagrangian grid which is independent from the employed Eulerian tetrahedral mesh. However, the quality of this moving grid is dependent on the local size of the Eulerian volumes hosting the free surface. The finer the Eulerian mesh is, the finer the Lagrangian resolution. This leads to a better capturing of the interface. This is illustrated in figure 7 where the lower tip of the vortex is better resolved by the finer meshes (figure 7, bottom).

Next, figure 8 illustrates the influence of the employed mesh on the quality of the global flow pattern. The represented iso-surfaces correspond to the instantaneous Q-criterion fields at  $t^* = 118$ . Comparing with figure 1 of [8], it is clearly shown that both, the forced and the free vortices are reproduced in all cases. From the colorbar legend which has been selected according to the values of the vertical velocity component  $u_3^*$ , it can be noted that global flow pattern is correctly described with all meshes. The central forced vortex convects the fluid particles from the free surface to the bottom, while the free vortices retake the fluid upward. However, the effect of the mesh refinement is obvious where the low resolution on the three coarsest meshes is clearly shown. Qualitatively, the resolution with Mesh 5 and Mesh 6 is almost the same.

The complexity of the flow illustrated in figure 8 makes it necessary to qualify the LES resolution. As followed and illustrated in [29], the ratio of the SGS viscosity to the kinematic viscosity serves as a good indicator on the quality of the resolved LES and importance of the turbulence in the configuration. In figure 9 (left to right, top to bottom), the ratio  $\nu_{\text{SGS}}/\nu$  is shown for all cases by the instantaneous iso-contours at  $t^* = 118$  in the two mid-vertical planes ( $\theta^* = 0$  and  $1/4$ ).

In all cases, the iso-contours show that the highest  $\nu_{\text{SGS}}/\nu$  ratios are situated in the liquid phase and along the central region of the reactor within the forced vortex, in the vicinity of the rotating magnetic rod and at the helical rotating free vortices. This behavior is rather expected as far as, by construction, the WALE SGS model is related to the macroscopic velocity gradients that are significant in these regions. However, the influence of the mesh is clearly noted where the max ratio of  $\nu_{\text{SGS}}/\nu$  decreases from 300 for Mesh 1 to 30 with Mesh 6, which is equivalent to a decrease of about 90% relative to the reference mesh. Maximum ratios of 50 and 30 obtained with Mesh 5 and Mesh 6 are reasonable in the framework of LES. Greater values can indicate that the numerical resolution is not fine enough.

Performing an LES which is implicit with respect to a mesh means that the solution approaches the DNS one as  $\nu_{\text{SGS}}/\nu$  tends to 0. In this framework, estimating the smallest Kolmogorov length scale can serve in identifying how far the solution is from that of the DNS. The turbulent Kolmogorov length scale is estimated to

$$\eta_{\text{LES}} = (\nu^3/\epsilon_{\text{LES}})^{0.25}, \quad (9)$$

where the instantaneous total dissipation rate is evaluated in terms of the symmetrical part of the resolved stress tensor  $S$  as

$$\epsilon_{\text{LES}} = 2(\nu_{\text{SGS}} + \nu)(S_{ij}S_{ji}). \quad (10)$$

The ratio of the employed mesh size  $\delta$  to  $\eta_{\text{LES}}$  is illustrated at  $t^* = 118$  by the instantaneous iso-contours in the same two mid-vertical planes for all cases (figure 10, left to right, top to bottom). It is clearly shown that the significant ratios are situated in the same spatial positions as those of  $\nu_{\text{SGS}}/\nu$  (figure 9), and thus illustrating the strong turbulence intensity in these regions. Although the ratio  $\delta/\eta_{\text{LES}}$  decreases by moving from the coarsest to the finest mesh, the maximum ratio 90 recorded

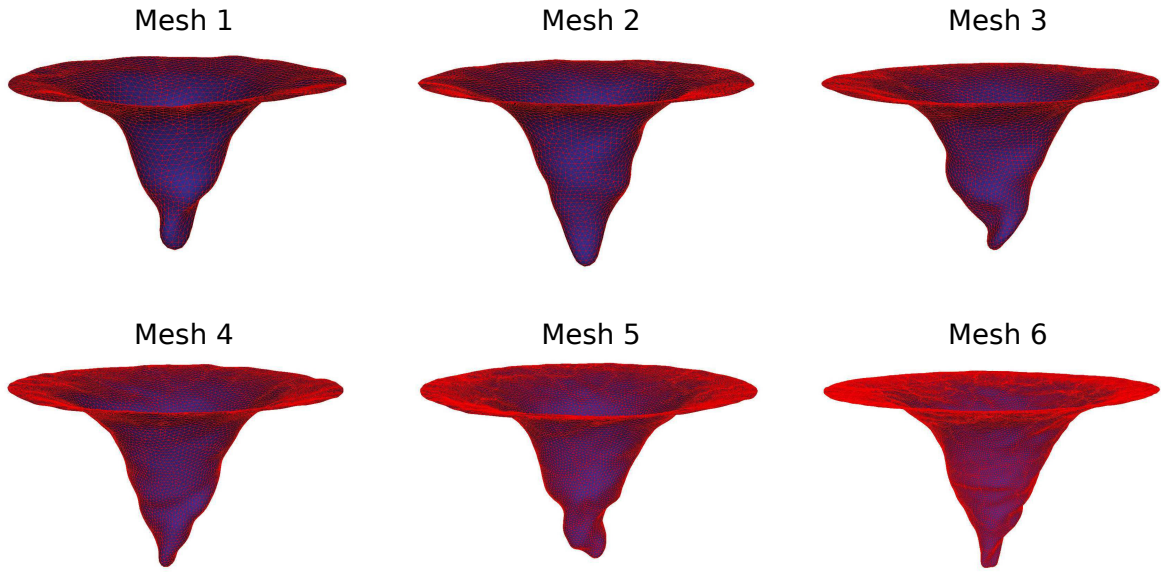


Figure 7: Instantaneous visualization of the vortex formed at the free-surface and its corresponding Lagrangian mesh illustrating the influence of the mesh. Left to right, top: Mesh 1, Mesh 2 and Mesh 3. Left to right, bottom: Mesh 4, Mesh 5 and Mesh 6.

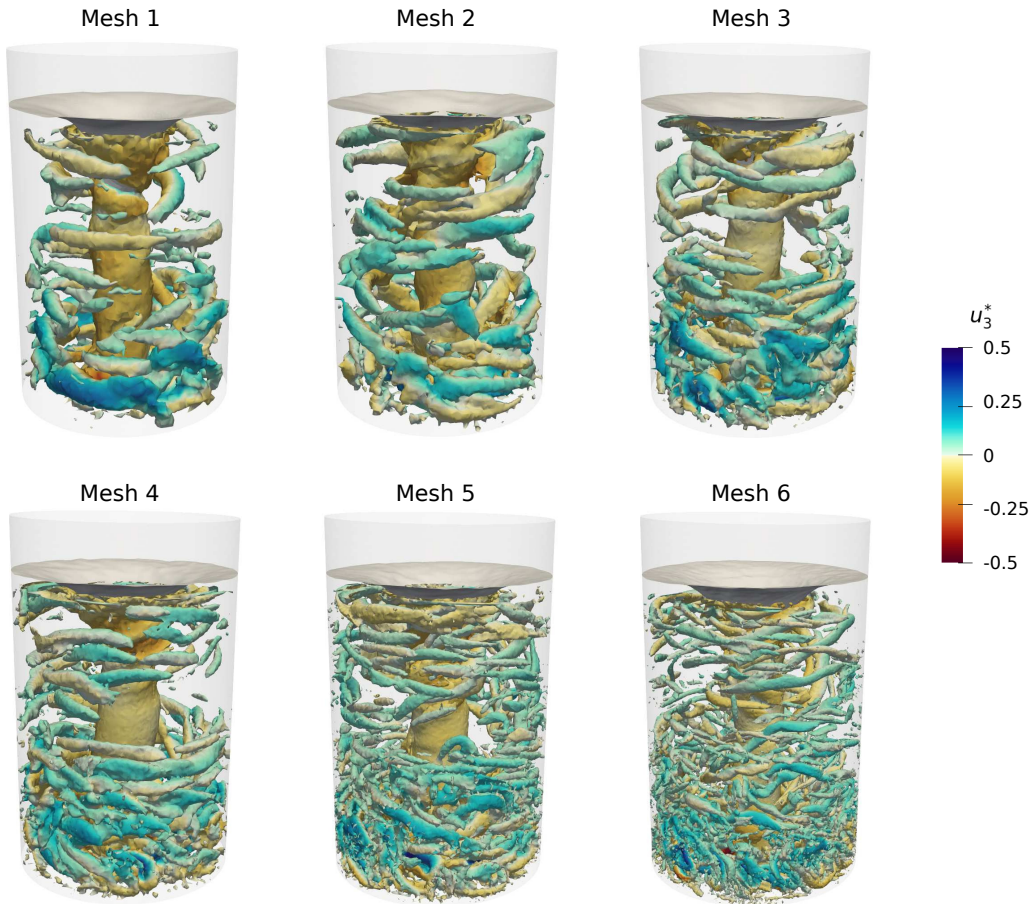


Figure 8: Instantaneous iso-surfaces of the Q-criterion colored by the vertical velocity component  $u_3^*$  at  $t^* = 118$  illustrating the mesh influence on the quality of the forced and free vortices. Left to right, top: Mesh 1, Mesh 2 and Mesh 3. Left to right, bottom: Mesh 4, Mesh 5 and Mesh 6.

with Mesh 6 explains how the reference mesh is even still far from what is required to perform a DNS.

Further investigations on the quality of the performed LES

could be achieved by estimating the turbulence length scale of Taylor  $\lambda_T$ . This is an intermediate length scale at which the effect of the viscosity  $\nu$  on the motion of turbulent eddies is firstly

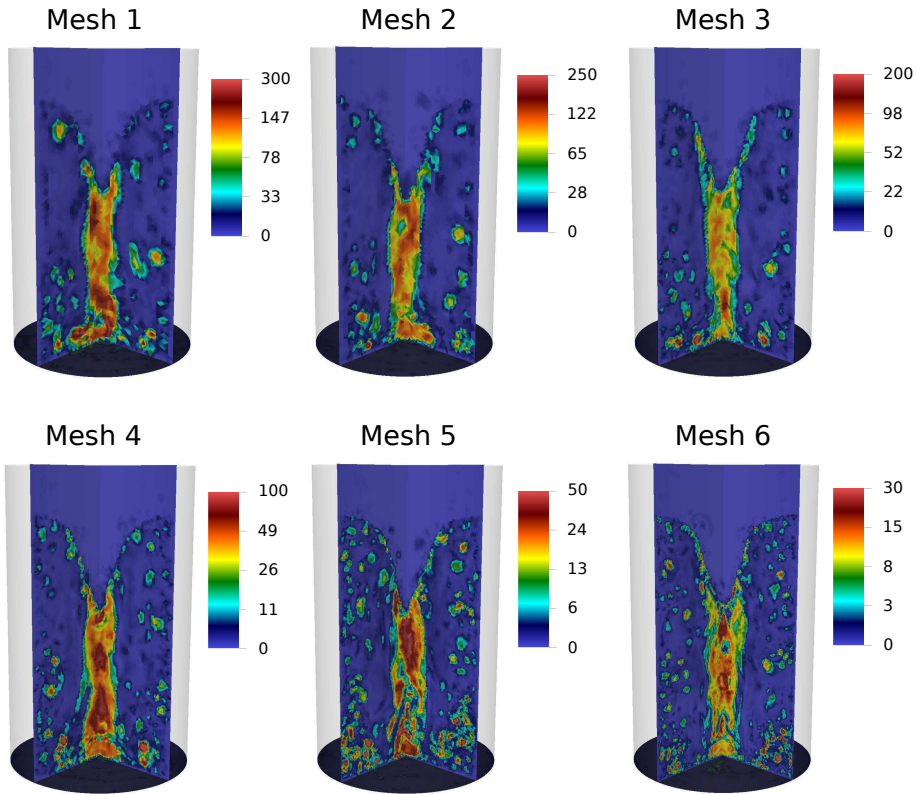


Figure 9: Instantaneous iso-contours of the SGS-to-laminar viscosity ratio  $\nu_{SGS}/\nu$  at  $t^* = 118$  in the two mid-vertical planes ( $\theta^* = 0$  and  $1/4$ ). Left to right, top: Mesh 1, Mesh 2 and Mesh 3. Left to right, bottom: Mesh 4, Mesh 5 and Mesh 6.

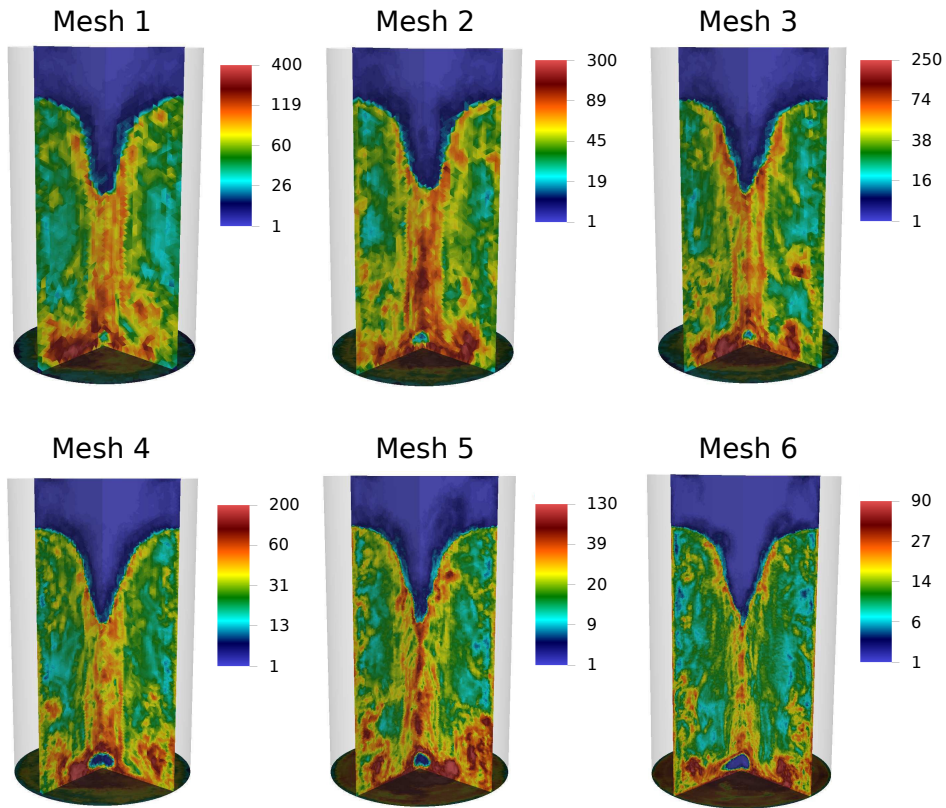


Figure 10: Instantaneous iso-contours of the estimated ratio of the employed mesh size  $\delta$  to  $\eta_{LES}$  in the two mid-vertical planes ( $\theta^* = 0$  and  $1/4$ ) at  $t^* = 118$ . Left to right, top: Mesh 1, Mesh 2 and Mesh 3. Left to right, bottom: Mesh 4, Mesh 5 and Mesh 6.

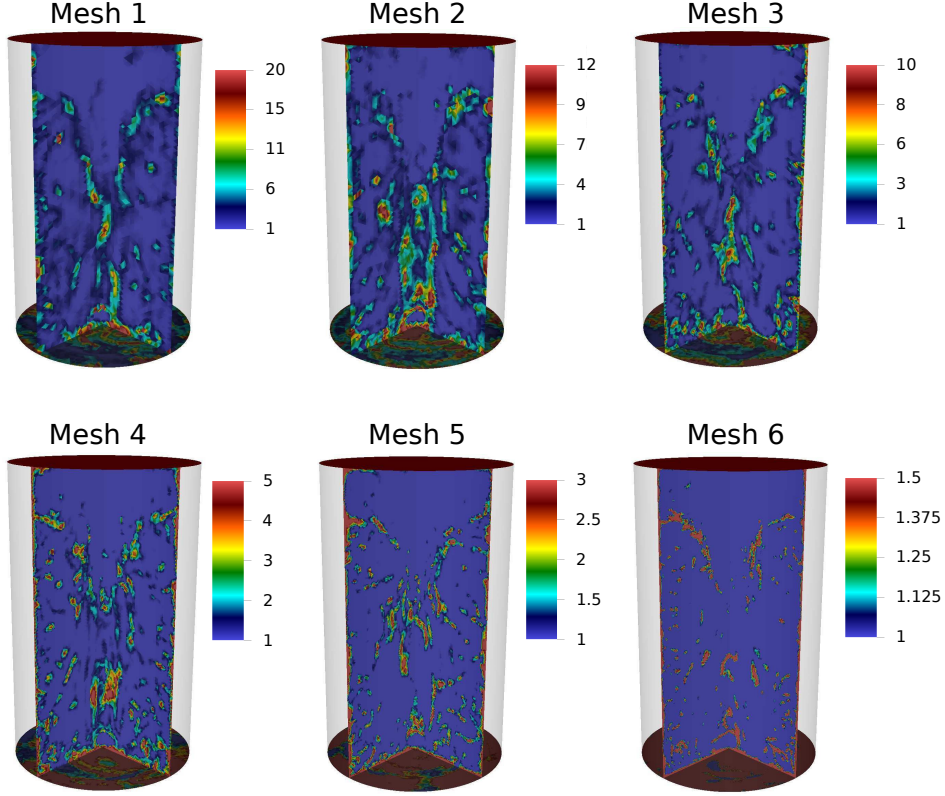


Figure 11: Instantaneous iso-contours of the estimated  $\delta/\lambda_T$  ratio in the two mid-vertical planes ( $\theta^* = 0$  and  $1/4$ ) at  $t^* = 118$ . Left to right, top: Mesh 1, Mesh 2 and Mesh 3. Left to right, bottom: Mesh 4, Mesh 5 and Mesh 6.

noted. Length scales larger than  $\lambda_T$  are not strongly affected by the viscosity and are generally referred to as the inertial range (high Re numbers). Below the Taylor scale, the turbulent motions are subject to strong viscous forces and kinetic energy is dissipated into heat. These shorter length scale motions are situated in the dissipation range situated at the end of the Kolmogorov power spectrum [13].

The turbulent micro-scale of Taylor is estimated in terms of the turbulent kinetic energy  $\mathcal{K}^t = \frac{1}{2} \sum_{i=1}^3 u_i' u_i'$  as

$$\lambda_T = (10 \mathcal{K}^t \nu / \epsilon_{\text{LES}})^{0.5}. \quad (11)$$

In the same planes considered previously, the ratio of the employed mesh size  $\delta$  to  $\lambda_T$  is illustrated in figure 11 by the iso-contours at  $t^* = 118$  (Mesh 1 to 6 from left to right, top to bottom). Clearly, the ratio decreases with the refinement of the mesh to reach a value of 3 starting from Mesh 5.

Such a reasonable ratio indicates that the employed mesh is at most 3 times larger than the turbulent Taylor micro scales, and then its quality is good. For Mesh 6, the maximum ratio is even smaller and reads 1.5, meaning that the mesh size is almost at the scale of the viscosity dissipation dominance. In conclusion, it can be stated that the performed LES is satisfactorily well resolved and that a reference solution is presented.

#### 4.2. Quantitative influence

To illustrate the quantitative influence for which the solution becomes somehow independent of the employed mesh, 576

uniformly distributed probes are considered in the  $(r, \theta, z)$  reference frame; 6 along the radial direction  $r$ , at 8 positions of  $\theta$  covering the whole domain and 12 along  $z$ . A 2D top-view exhibiting the spatial positions of the probes in the horizontal  $r\theta$ -plane is illustrated in figure 12.

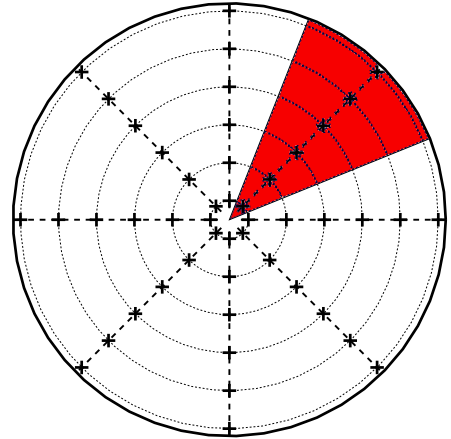


Figure 12: 2D top view exhibiting the spatial positions of the probes in the horizontal  $r\theta$ -plane of the RVE. Red sector illustrates the cells used to estimate the L2 norm of a considered quantity.

For each simulation, the velocity field  $\mathbf{u} = (u_1, u_2, u_3)$  is recorded on each of the 576 probes with a frequency  $f$  ( $f^* = f/N \approx 172$ ). The analysis is carried out on the statistical field defined in equations (7) and (8) with  $t_{\text{start}}^* = 25$ . Recall that the

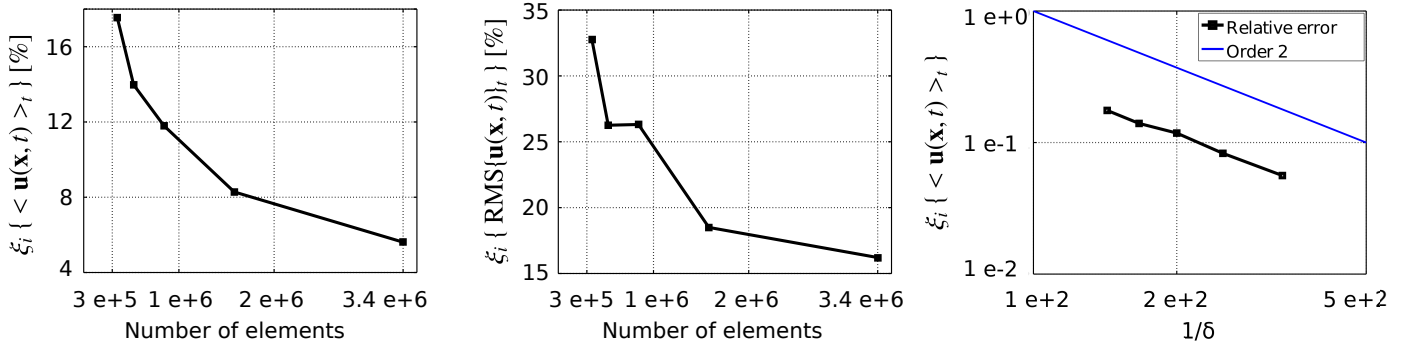


Figure 13: Evolution of the convergence relative error relative to Mesh 6. Left: time averaged field, middle: RMS field, right: time averaged field versus  $1/\delta$  in a log scale showing the second order convergence.

reference mesh is Mesh 6, referred to it inhere by the upper-script  $\{\text{ref}\}$ . For a considered variable  $\varphi$ , the L2 norm is defined as

$$\|\varphi\|_{L2} = \left( \sum_{i=1}^{576} \varphi^2 V_i / V \right)^{1/2}, \quad (12)$$

where  $V$  is the fluid's total volume and  $V_i$  the volume of the cell associated to the probe  $i$ , seen in 2D as a part of the red sector sketched in figure 12. Relative to the reference mesh, a difference quantity  $\xi$  is defined as

$$\xi_i \{ \varphi(\mathbf{x}) \} = \|\varphi^{\text{Mesh } i}(\mathbf{x}) - \varphi^{\text{ref}}(\mathbf{x})\|_{L2} / \|\varphi^{\text{ref}}(\mathbf{x})\|_{L2}, \quad (13)$$

where  $\varphi(\mathbf{x}) = \{ \langle \mathbf{u}(\mathbf{x}, t) \rangle_t, \text{RMS}\{\mathbf{u}(\mathbf{x}, t)\}_t \}$ . The variation of  $\xi_1$  to  $\xi_5$  is presented in figure 13 as a function of the total grid number for both, the mean (left) and RMS (middle) quantities.

For the velocity time averaged field, the graph points how the difference relative to Mesh 6 decreases with the mesh refinement. Starting with a  $\xi_1 \{ \langle \mathbf{u}(\mathbf{x}, t) \rangle_t \}$  about 18%, the quantitative decrease show that the difference at Mesh 5 is reduced to about 6%. Similarly, a decrease is noted on the RMS fields (figure 13, middle) from about 34% to 16%. However, the rate of the variation in this case is rather slower than that observed on the averaged field. The same observation had been stated in [30] and is more or less an issue of single versus second order moment convergence. Moreover, the step noted on the profile between Mesh 2 and Mesh 3 is probably related to the homogeneity of the mesh where it seems that the refinement is not linear between them.

The evolution of  $\xi_i \{ \langle \mathbf{u}(\mathbf{x}, t) \rangle_t \}$  versus  $1/\delta$  is shown with a log scale in figure 13 (right). On the same figure, the second order convergence is illustrated with a solid blue line. Clearly, the evolution of the difference relative to Mesh 6 is of a second order, which is coherent with the theory since a second order scheme is used for the spatial discretization.

It is extremely important here to emphasize that the evaluated quantities contains not only the difference introduced by the mesh, but also those induced by the LES modelling and those related to the spatial/temporal schemes errors. Moreover, it has been figured out that the highest difference values are located in the vicinity of the stirrer where the flow is extremely

turbulent. Much smaller values are recorded elsewhere in the reactor. In conclusion, it can be stated that the LES solution obtained with Mesh 5 are satisfactorily close to those of Mesh 6. Unless otherwise stated, the results are presented in the sequel from Mesh 5. The satisfactorily qualitative resolution obtained with Mesh 6 and discussed previously regarding the viscosity ratio, Taylor micro-scales and free-surface vortex resolution enhance the choice.

## 5. Flow pattern

In this section, the flow pattern of the RVE is presented. Recall that the rotational motion of the magnetic rod at the bottom of the tank makes the tangential velocity component  $u_2$  dominant in the study.

### 5.1. Instantaneous turbulent flow structures

The instantaneous flow structure at  $t^* = 150$  is firstly illustrated in figure 14 (top) by the different velocity components in the mid-vertical plane ( $\theta^* = 0$ ). From the iso-contours, it can be stated that the flow is highly turbulent with a  $u_2$  dominance. The highest values of  $u_1^*$  and  $u_3^*$  are situated near the rod at the bottom and near the free-surface at the top. At the top, the distribution is rather coherent with the shape of the vortex formed at the free-surface. The tangential distribution is almost symmetrical in the RVE. The axis-symmetry is confirmed by the velocity magnitude  $|\mathbf{u}^*|$  iso-contours and vectors, either in the same vertical plane (figure 14, bottom), or in two horizontal planes situated at  $z^* = 0.03$  and  $z^* = 0.27$  (figure 15).

In addition to the vicinity of the rod, the maximal  $u_2^*$  values are predicted around the central region of the reactor; the forced vortex zone. The tangential velocity is zero in the reactor axis, reduces in the free vortex zone and trend to zero at the outer wall. A quantitative illustration is presented in figure 16 where the time evolution of  $u_2^*$  is considered at four pair-wise symmetrical probes in the central region at  $r^* = 0.18$  (figure 16, left) and in the free vortex region at  $r^* = 0.7$  (figure 16, right). The probes are located at a height  $z^* = 0.27$ .

The profiles show how the tangential velocity values reduce in the free vortex, compared to those in the central zone. Moreover, the highly fluctuating profiles show that the turbulence

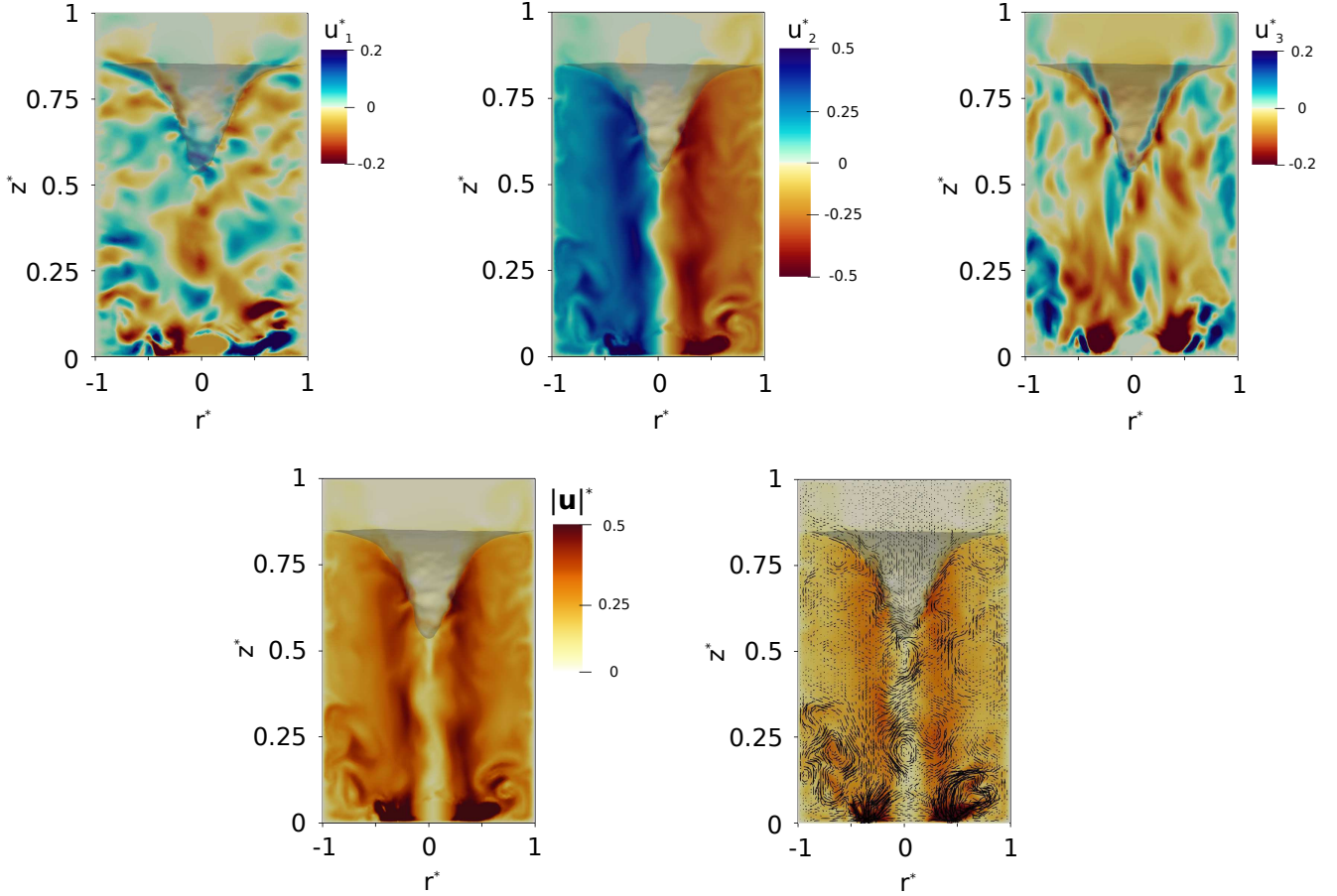


Figure 14: Instantaneous flow pattern illustrated by the velocity iso-contours at  $t^* = 150$  in the mid-vertical plane ( $\theta^* = 0$ ). Top: radial velocity  $u_1^*$  (left), tangential velocity  $u_2^*$  (middle), axial velocity  $u_3^*$  (right). Bottom: velocity magnitude  $|\mathbf{u}|^*$  (left), vector field (right).

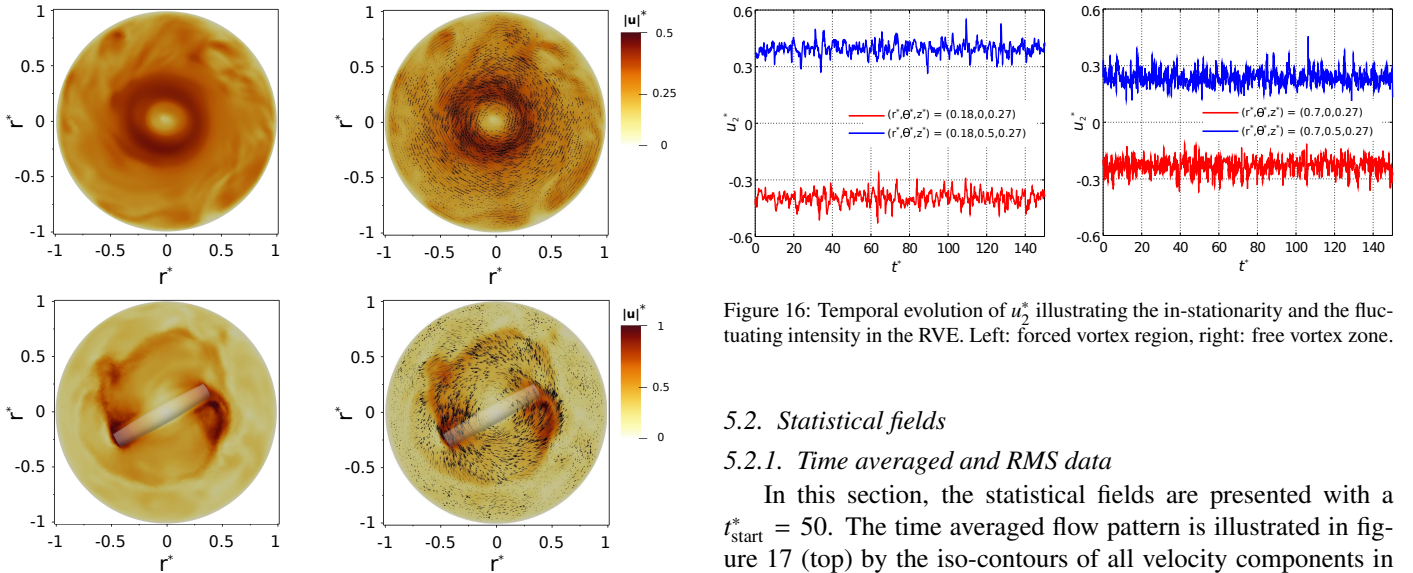


Figure 15: Instantaneous flow pattern illustrated by the dimensionless velocity magnitude  $|\mathbf{u}|^*$  iso-contours (left) and vectors (right) at  $t^* = 150$  in two horizontal planes. Bottom:  $z^* = 0.03$ , top:  $z^* = 0.27$ .

intensity is not identical in the RVE and that the flow is completely unsteady.

Figure 16: Temporal evolution of  $u_2^*$  illustrating the in-stationarity and the fluctuating intensity in the RVE. Left: forced vortex region, right: free vortex zone.

## 5.2. Statistical fields

### 5.2.1. Time averaged and RMS data

In this section, the statistical fields are presented with a  $t_{\text{start}}^* = 50$ . The time averaged flow pattern is illustrated in figure 17 (top) by the iso-contours of all velocity components in the mid vertical  $rz$ -plane at  $\theta^* = 0$ . A good visible symmetrical distribution is noted on all velocity components.

The distribution of  $\langle u_2^* \rangle_t$  is almost uniform along the vertical direction (figure 17, top-middle). Largest values are located in the central region and near the rod, trend to zero when approaching the central axis and the walls. A similar uniform distribution with respect to  $z$  is noted on the  $\langle u_3^* \rangle_t$  field. Neg-

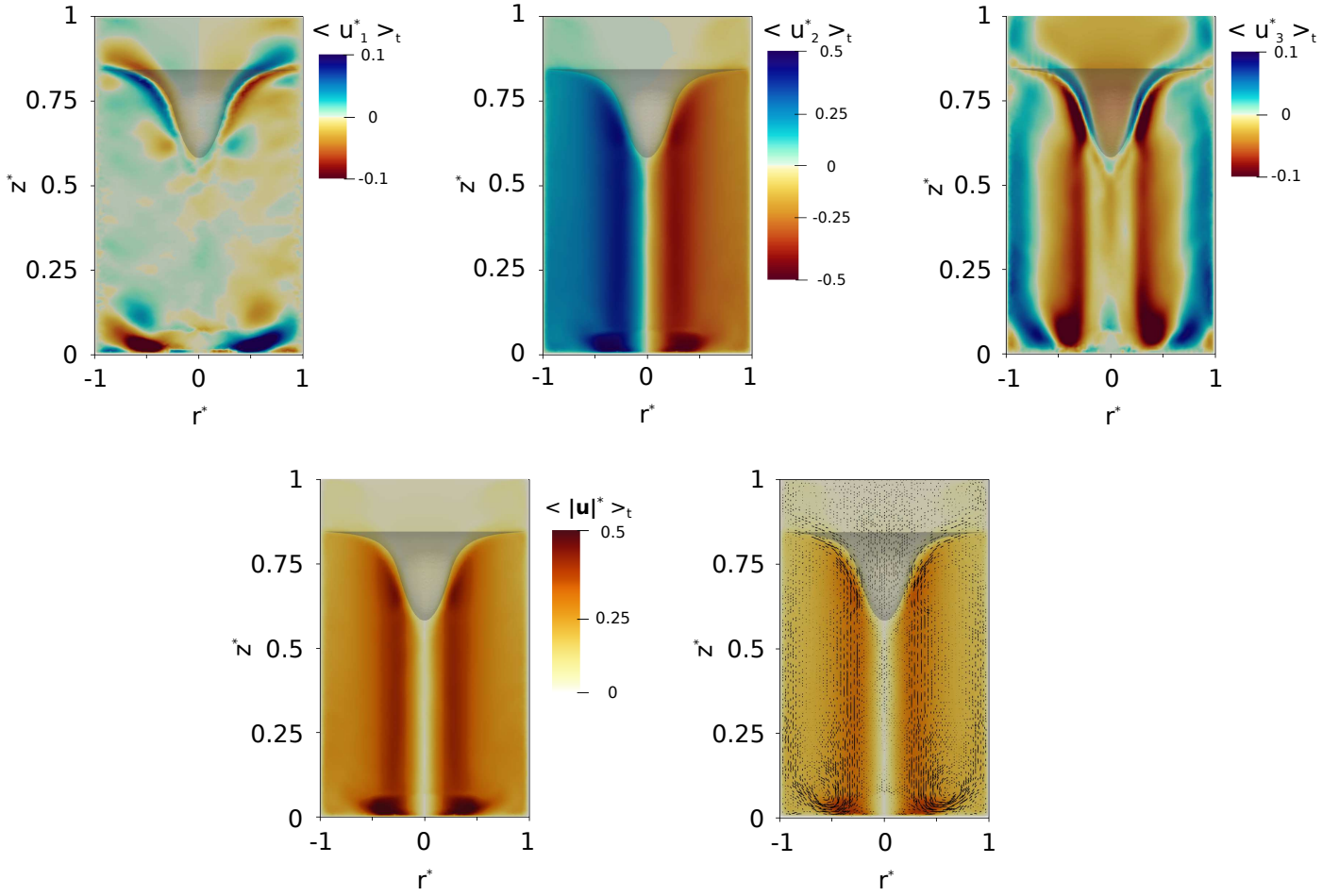


Figure 17: Time averaged flow pattern illustrated by the velocity iso-contours in the mid-vertical  $rz$ -plane ( $\theta^* = 0$ ). Top: radial velocity  $\langle u_1^* \rangle_t$  (left), tangential velocity  $\langle u_2^* \rangle_t$  (middle), axial velocity  $\langle u_3^* \rangle_t$  (right). Bottom: velocity magnitude  $\langle |\mathbf{u}^*| \rangle_t$  (left), vector field (right).

ative vertical velocities are situated in the central region to convect the fluid in the downward direction. Near the walls, the values are positive to push the fluid upward with the free vortices (figure 17, top-right). In this cycle,  $\langle u_1^* \rangle_t$  plays an important role at the top near the free-surface, and at the bottom near the edges of the rod. This behavior is of a particular interest in the precipitation process and in enhancing the mixing. Otherwise, the values of the radial velocity are almost negligible (figure 17, top-left).

The velocity magnitude  $\langle |\mathbf{u}^*| \rangle_t$  is illustrated by the iso-contours and the vector field in the same vertical plane (figure 17, bottom) and in figure 18 for the same two horizontal planes considered previously. As expected, the distribution is almost the same as that of  $\langle u_2^* \rangle_t$ . From the horizontal distribution and mainly in the plane situated at  $z^* = 0.27$ , it is clearly noted that the forced vortex occupies a non-negligible volume in the RVE. A better illustration is provided in figure 19 from a 3D view. Here, the vector field, the velocity stream lines and the Q-criterion iso-surfaces are served and colored by the values  $u_3^*$ . The symmetry of the flow, the downward motion at the center and the upward one in the far field, the forced vortex and the free one, in addition to the orientation of the flow are all noted.

Next, the velocity fluctuations are illustrated in figure 20 by

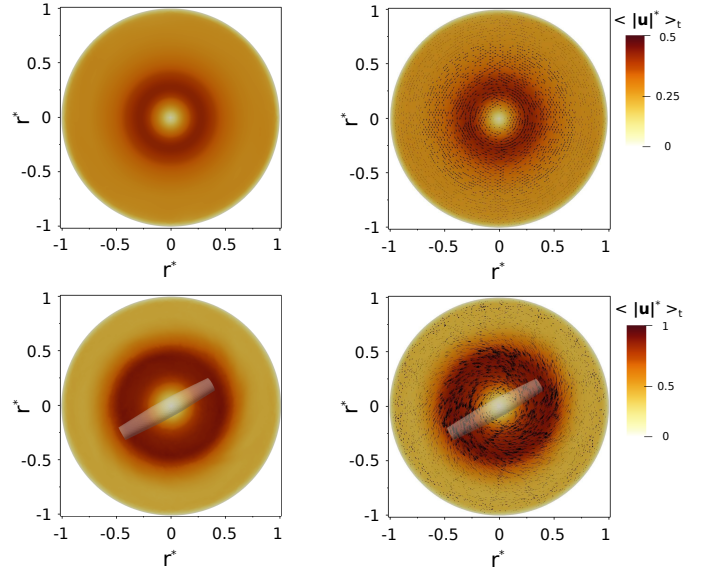


Figure 18: Time averaged flow pattern illustrated by the dimensionless velocity magnitude in two horizontal planes situated respectively at  $z^* = 0.03$  (bottom) and  $z^* = 0.27$  (top). Left:  $\langle |\mathbf{u}^*| \rangle_t$  iso-contours, right: vector field.

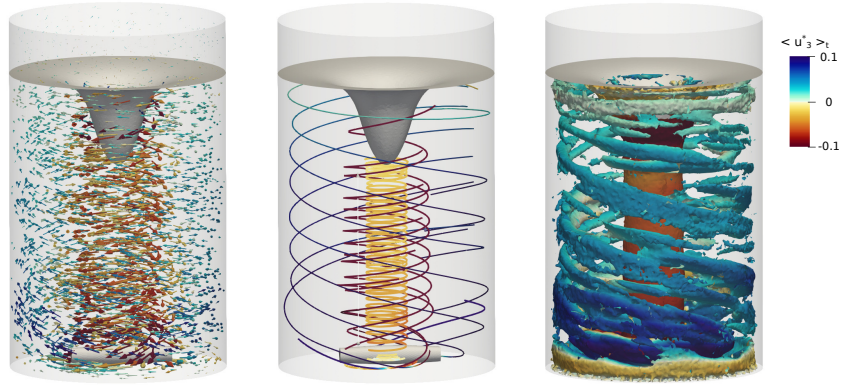


Figure 19: 3D time averaged flow pattern and turbulent structures. Left: vector field, middle: velocity streamlines and right: Q-criterion. The fields are colored according to values of  $u_3^*$  to describe the orientation of the ascending/descending flow motion.

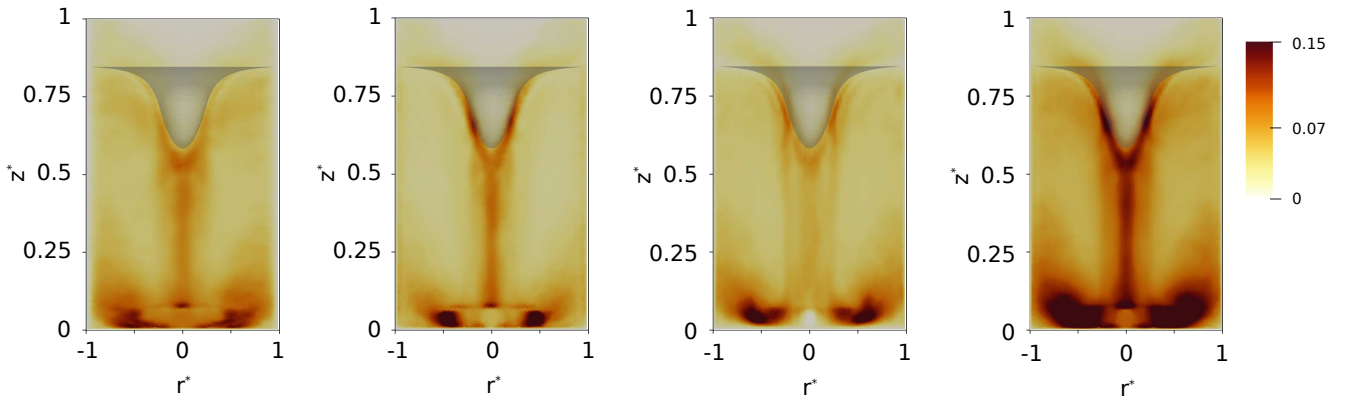


Figure 20: Velocity RMS iso-contours in the mid-vertical  $rz$ -plane ( $\theta^* = 0$ ). Left to right:  $\text{RMS}\{u_1^*\}_t$ ,  $\text{RMS}\{u_2^*\}_t$ ,  $\text{RMS}\{u_3^*\}_t$  and  $\text{RMS}\{|\mathbf{u}^*|\}_t$ .

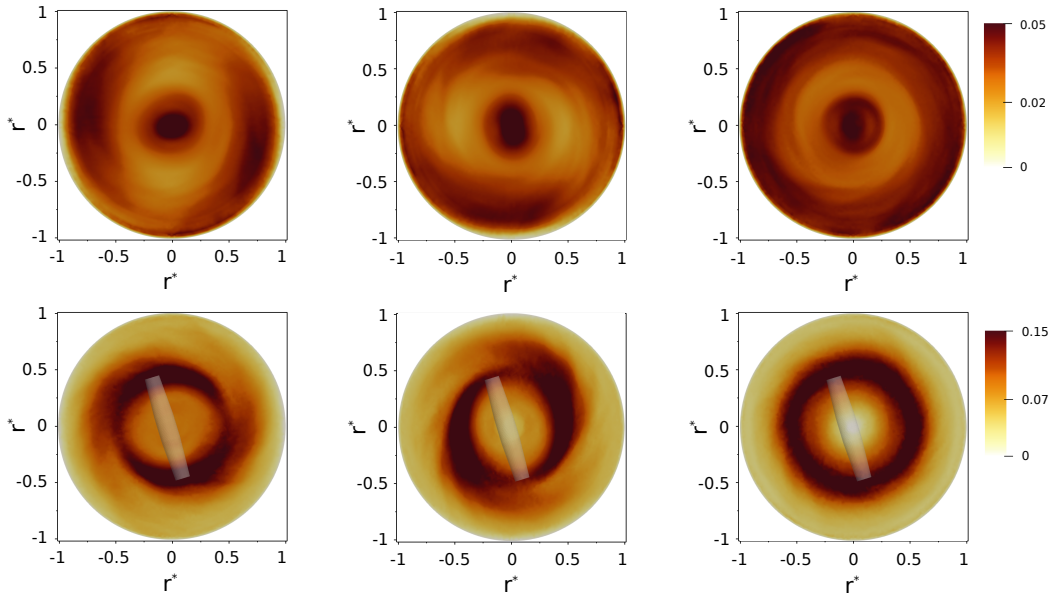


Figure 21: Velocity RMS iso-contours in two horizontal planes situated respectively at  $z^* = 0.03$  (top) and  $z^* = 0.27$  (bottom). Left to right:  $\text{RMS}\{u_1^*\}_t$ ,  $\text{RMS}\{u_2^*\}_t$  and  $\text{RMS}\{u_3^*\}_t$ .

the RMS iso-contours in the mid-vertical  $rz$ -plane ( $\theta^* = 0$ ). As shown for all components, the significant velocity fluctuations are situated at the bottom of the reactor near the magnetic rod at first, and then in the vicinity of the forced vortex and near

the water/air interface at second. To the contrary, the fluctuations intensity in the free vortices zone is much smaller. In the central axis of the reactor, the recorded RMS values are not negligible. However, since the velocity values are almost null at

this position, it can be stated that these RMS values weakly affect the flow structure. A numerical and/or physical reason can stand behind the presence of such oscillations along the axis. They might originate due to the turbulence and to the complete unsteadiness of the central axis position.

As the case of the time averaged fields, the RMS fields are also symmetrically distributed in the domain, with respect to the central axis. This is furthermore illustrated in figure 21 for the same horizontal planes considered previously. In all tangential directions, the highest oscillations take place near the stirrer as illustrated in the horizontal plane  $z^* = 0.03$  (figure 21, bottom). Regarding the higher  $r\theta$ -plane (figure 21, top), it is clear that the largest oscillations are located in the forced vortex and in the free one near the walls due to the fluid/wall interactions. Otherwise, a quite zone with small oscillating intensity takes place.

In the remaining part of this subsection, the quality of the statistical data is presented in terms of numerical accuracy (standard error of the mean) and convergence. In this framework, the analysis is carried out locally at six fixed probes situated in the mid-vertical  $rz$ -plane ( $\theta^* = 0$ ). The first three probes are chosen vertically in the forced vortex at  $r^* = 0.18$  and heights  $z^* = 0.03, 0.4, 0.8$ , while the other three are in the free vortex zone at  $r^* = 0.7$  and same heights.

### 5.2.2. Statistical accuracy

To define the numerical-statistical accuracy of the presented data, the approach used in [30] is followed where the standard error of the mean (SEM) is estimated. As detailed in [31, 32], SEM measures the dispersion of the sample mean around that of the population. Mathematically, the numerical-statistical accu-

racy presented here for the velocity magnitude field is estimated as

$$\text{Err}(\mathbf{u}) = \text{RMS}\{|\mathbf{u}(t)\}_t / \sqrt{\mathcal{N}}, \quad (14)$$

where  $\mathcal{N}$  denotes the number of independent samples and not the total number of sampling. As stated in [33], the number of independent samples can be easily deduced from the auto-correlation function (ACF) which is defined for a time lag  $\tau$  as

$$r(\tau)_{|\mathbf{u}|} = \langle |\mathbf{u}'(t) \cdot |\mathbf{u}'(t + \tau) \rangle_t / \langle |\mathbf{u}'(t) \cdot |\mathbf{u}'(t) \rangle_t. \quad (15)$$

The ACF profiles obtained at the six probes are shown in figure 22. It is shown that the correlation rapidly decreases in all cases with the dimensionless time delay  $\tau^*$ . At the lowest probe of the forced vortex, the periodicity of the profile describes the frequency at which the stirrer passes by this position.

A good quadratic polynomial is fitted around the origin and thus plotted on the same graphs (red lines). According to the definition of the Taylor's time micro-scale [13],  $\lambda_f$  is nothing but the intersection of the inscribed fitted parabola with the time delay axis. With the same sampling frequency considered previously in subsection 4.2, the number of correlated data is thus  $f\lambda_f$ .

Form this analysis, equation (14) is considered and the results are summarized in table 3. In all cases, it can be stated the smallest turbulent time scales of Taylor are situated at the lowest probe near the stirrer, and that they increase as the top of the reactor is approached. In accordance with the previous observations, the highest error value is near the extremity of the stirrer at the lowest probe in the free vortex zone. However, in general, the errors are very small and confirm the good quality of the presented data.

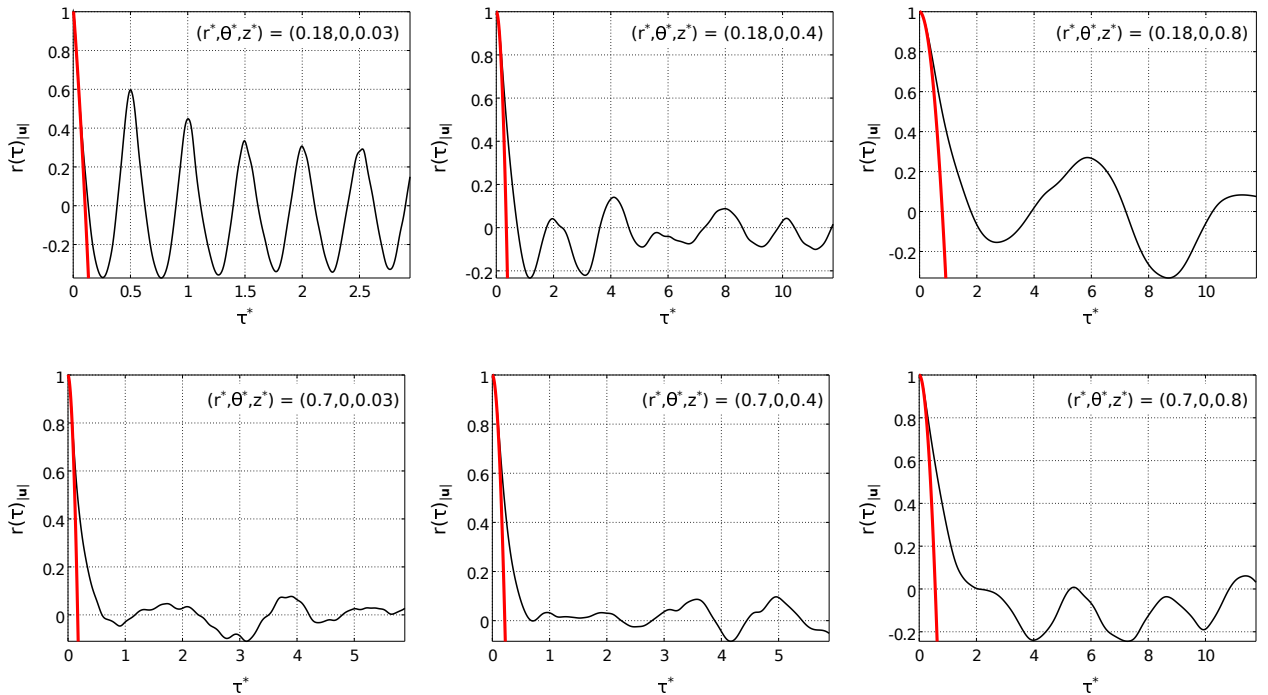


Figure 22: ACF( $|\mathbf{u}|$ ) at six probes in the mid-vertical  $rz$ -plane ( $\theta^* = 0$ ). Top: probes in the central zone, bottom: probes in the far field. Red line corresponds to the inscribed fitted parabola around the origin used to determine the Taylor micro-scale  $\lambda_f$ .

Probe $(r^*, \theta^*, z^*)$	Forced vortex			Free vortex		
	$(0.18, 0, 0.03)$	$(0.18, 0, 0.4)$	$(0.18, 0, 0.8)$	$(0.7, 0, 0.03)$	$(0.7, 0, 0.4)$	$(0.7, 0, 0.8)$
Taylor $\lambda_f^*$	0.13	0.4	0.9	0.16	0.23	0.63
Err( $ \mathbf{u} ^*$ )	$3.7 \times 10^{-3}$	$4.7 \times 10^{-3}$	$2.7 \times 10^{-3}$	$6.5 \times 10^{-3}$	$1.8 \times 10^{-3}$	$3.4 \times 10^{-3}$

Table 3: Numerical-statistical accuracy estimated from an auto-correlation analysis at six probes situated in the mid vertical  $rz$ -plane ( $\theta = 0$ ).

In the next part, the convergence of the statistical fields is illustrated in terms of increasing the number of accumulated data with the increasing time of the simulation. For completeness, the analysis is presented on both, the velocity magnitude and the pressure fields.

### 5.2.3. Statistical convergence

Figure 23 describes the time evolution of  $\langle |\mathbf{u}|^* \rangle_t$  and the reduced pressure  $\langle P \rangle_t - \rho g z$  at the six probes. The convergence of the mean quantities is clear where a plateau is reached in all cases by increasing the number of accumulated data. However, it can be stated that the convergence of the time-averaged quantities near the edge of the rod in the far field (black profiles in the right-pair) is slower than in other cases; to compare  $t^* \approx 80$  with  $t^* \approx 100$ . This is coherent with the previous discussion since the largest statistical error is recorded at this position.

We take advantage from the profiles of figure 23 to provide some quantitative information regarding the flow in the RVE. Concerning the velocity magnitude, it is clear how the same values are almost recorded in the forced vortex (lower two probes of figure 23, top-left). At the third probe (red profile), the val-

ues are smaller by about 85% since this probe is situated in the air phase above the free-surface vortex. In the far field (figure 23, top-right), the values decrease gradually by moving from the bottom to the top of the reactor. The decrease is not that important and reads about 10% at most between two consecutive levels.

Regarding the reduced pressure, it is clear that the values are almost identical in the forced vortex as illustrated at the lower probes of figure 23 (bottom-left). At the higher probe which is above the free surface, the reduced pressure is higher and almost constant. In the far fields (figure 23, bottom-right), the reduced pressure values increase gradually with  $z$ .

Figure 24 illustrates the local convergence of the RMS fields where a plateau is reached in all cases. However as expected, it can be stated that the convergence is slower than the previous case of the mean quantities. In the far field, the convergence at the upper two probes far away from the stirrer is the fastest. This is illustrated by the red and blue profiles in figure 24 (right) where the plateau is reached at  $t^* \approx 80$ . To the contrary, at least  $t^* \approx 130$  is required at the remaining points.

As stated previously, the largest velocity oscillations take place near the stirrer at the lowest probes (black profiles), and

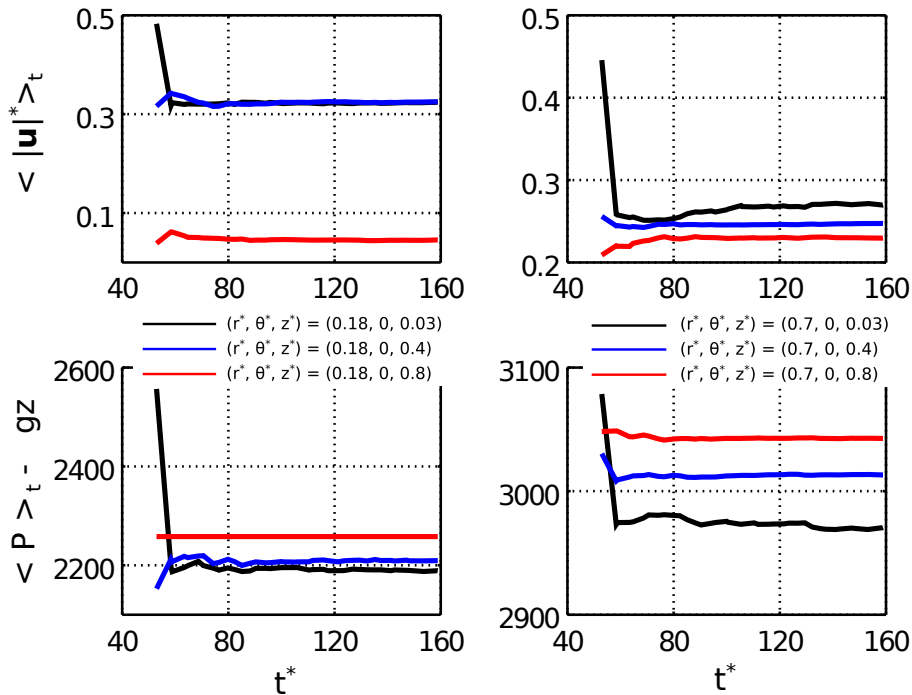


Figure 23: Time evolution of the time-averaged quantities illustrating the local convergence of the statistical data at six fixed probes in the mid-vertical  $rz$ -plane ( $\theta = 0$ ). Top-pair: dimensionless velocity magnitude  $\langle |\mathbf{u}|^* \rangle_t$ , bottom-pair: reduced pressure  $\langle P \rangle_t - \rho g z$ . Left-pair: central region, right-pair: far field.

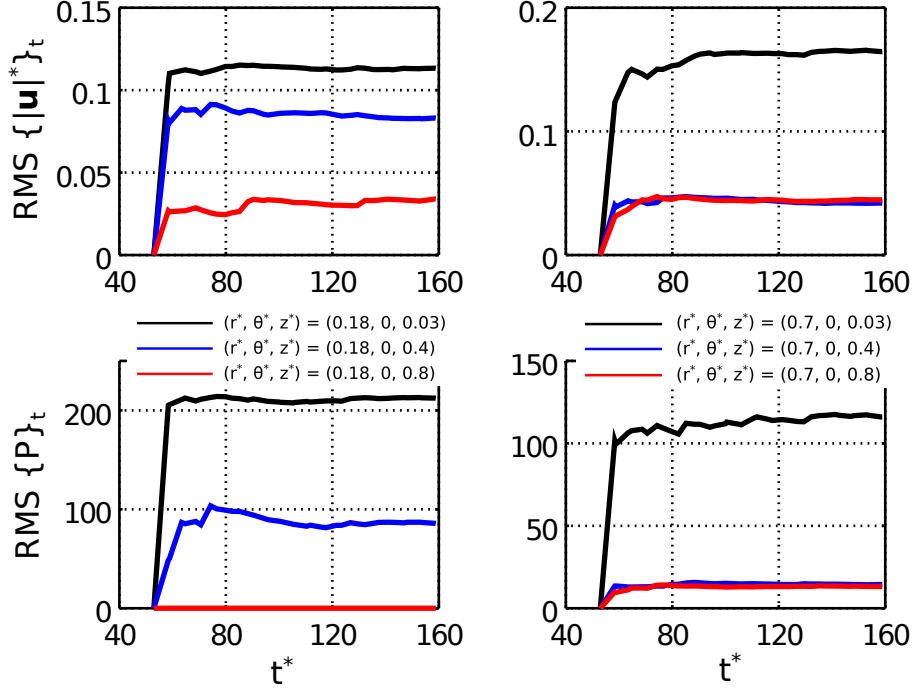


Figure 24: RMS fields time evolution illustrating the local convergence of the statistical data at six fixed probes in the mid-vertical  $rz$ -plane ( $\theta = 0$ ). Top-pair: dimensionless velocity magnitude  $\text{RMS}\{|u^*|}_t$ , bottom-pair:  $\text{RMS}\{P\}_t$ . Left-pair: central region, right-pair: far field.

are mostly significant near the extremity of the rod (figure 24, top-right). The oscillations are reduced along the two higher probes. However, their intensity decreases in the forced vortex as the free surface is approached, while being almost of the same order in the far field.

Similarly, the largest pressure oscillations take place at the bottom of the tank, and that they decrease in the upper part of the tank. In the forced zone, the RMS is zero at the highest probe as far as a constant mean has been recorded previously (probe situated above the free surface). In the free vortex zone, the pressure oscillations along the higher two probes are almost of the same importance.

## 6. Comparisons and LES validations

This section is devoted to the validation of the LES results. First, comparisons versus measurements from the literature are presented. Here, the dimensions of the free-surface vortex and the critical radius of the forced vortex are mainly concerned. Afterwards, the statistical data are compared versus the LDV measurements for validations.

### 6.1. Free-surface vortex and forced / free vortex boundary

To illustrate the efficiency of the DFT algorithm in tracking the free-surface, the time variation of the vortex spatial position is considered. In figure 25, the time evolution of the maximal recorded vortex height and the minimal one (vortex tip) is presented. Due to the turbulence, it can be clearly noted how the maximum position is almost stable (about  $z^* = 0.86$ ), while oscillating in the minimal positions around  $z^* = 0.52$ . In average, the dimensionless height of the predicted vortex is about 0.34.

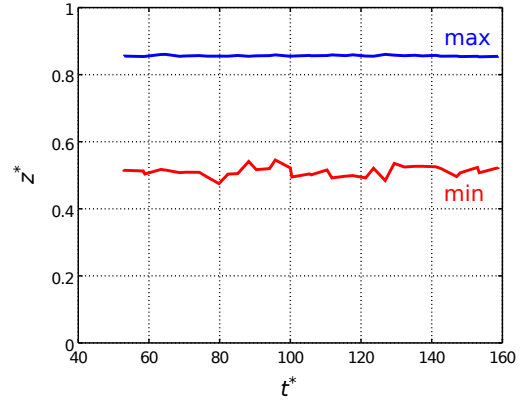


Figure 25: Time evolution of the maximum/minimum free surface positions.

Compared to the Nagata's theory [6], figure 26 shows both qualitative and quantitative comparisons. Qualitatively, a 3D visualization compares the LES vortex (red iso-surfaces) at two time instants with a Nagata profile (black iso-surface) is shown. Quantitatively speaking, the spatial position of the vortex in the mid-vertical  $rz$ -plane ( $\theta = 0$ ) is illustrated in the right of the figure. The red scatter corresponds to the LES at several snapshots, while the black solid profile is the one from Nagata. The good agreement is clear, thanks to the DFT method.

Next, the critical radius  $r_c$  is considered to validate further the LES prediction. Recall  $r_c$  is the boundary separating the forced from the free vortex. According to the Rankine's mathematical description of the vortex [7], the tangential velocity increases linearly with the radial direction  $r$  in the zone of forced vortex. However, the mean velocity is inversely propor-

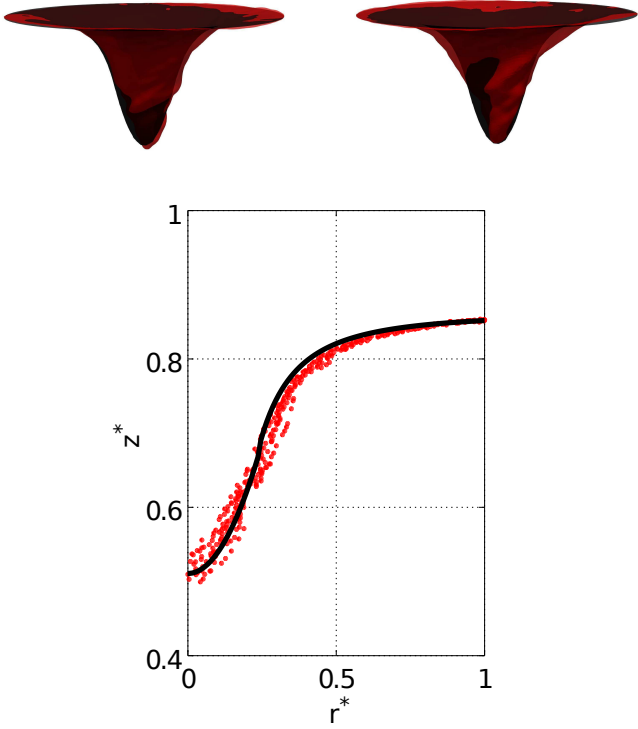


Figure 26: Top: 3D qualitative comparison of the LES/Nagata vortex at two time instants, bottom: quantitative comparison in the mid-vertical  $rz$ -plane ( $\theta^* = 0$ ). LES profiles in red while Nagata's profile in black.

tional to  $r$  in the free vortex zone. Mathematically, the behavior is described as

$$\langle u_2^* \rangle_t = \dot{\theta}^* r^* \quad : \quad r \leq r_c, \quad (16)$$

$$\langle u_2^* \rangle_t = K/(r^*)^n \quad : \quad r > r_c, \quad (17)$$

where  $\dot{\theta}$  is the angular velocity defined in its dimensionless form as  $\dot{\theta}^* = T\dot{\theta}/2\mathbf{u}_r$ , while  $K$  is a real constant.

In figure 27, the time averaged radial profile of the tangential velocity component  $\langle u_2^* \rangle_t$  at  $z^* = 0.4$  is sketched. A linear fit near the origin is considered on the same figure by the dashed blue line. The coefficient obtained by the linear regression gives  $\dot{\theta} = 0.987(2\pi N) \approx 2\pi N$  which is very well close to the theory according to the definition of the angular velocity. In the free vortex zone, the fit lead to a value of  $n = 0.69$  (see red dashed line on the same figure). This is coherent with the experimental value  $n \approx 0.7$ . Due to the presence of the viscous boundary layer near the wall, the sharp decay of the velocity values is clearly noted at the end of the profile.

The intersection of the two fitted profiles defines the boundary between the two zones and thus  $r_c$ . Here, the obtained value is  $r_c^* \approx 0.243$  and leads to a ratio  $2r_c/D \approx 0.52$ . To estimate the ratio  $2r_c/D$ , Nagata and Le Lan [34] propose two correlations respectively as

$$2r_c/D = \text{Re}_s/(2.11\text{Re}_s - 15850), \quad (18)$$

$$2r_c/D = \text{Re}_s/(2.27\text{Re}_s - 20630). \quad (19)$$

In table 4, the values obtained from the correlations, in addition to those measured experimentally at CEA Marcoule, are summarized where a good agreement is well noted.

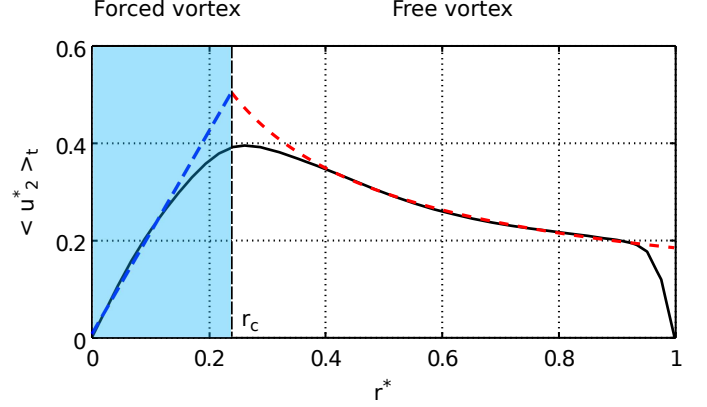


Figure 27: Time averaged radial profile of the tangential velocity component  $\langle u_2^* \rangle_t$  at  $z^* = 0.4$  employed to identify the value of the critical radius  $r_c$ . Forced vortex: dashed blue profile obtained by a linear fit near the origin, free vortex: dashed red profile obtained by an inversely proportional fit.

	LES	Nagata	Le Lan	Experiment
$2r_c/D$	0.52	0.53	0.51	0.48

Table 4: Comparisons of the LES prediction versus theoretical/experimental values regarding the length of the critical radius in the RVE.

## 6.2. Validations versus the LDV experiment

In this part, the statistical fields are compared with the LDV measurements from the experiment carried out at CEA Grenoble [8]. Time-averaged and RMS comparisons of all velocity components are provided in vertical and/or radial profiles situated in the mid-vertical  $rz$ -plane ( $\theta = 0$ ). The radial profiles are considered at three heights  $z^* = 0.03, 0.28$  and  $0.47$  for the first and third velocity components ( $u_1$  and  $u_3$ ), while at  $z^* = 0.1, 0.28$  and  $0.47$  for the tangential velocity ( $u_2$ ). For  $u_1$  and  $u_3$  components, the vertical profiles are considered at  $r^* = 0.6$  and  $0.8$ .

Figure 28 describes the comparisons regarding the radial velocity component along the three radial profiles. Black solid lines corresponds to the LES solution, while the LDV values are presented with the blue symbols. The comparison is very good and the profiles are almost superposed, specially on highest profiles far from the rod. Near the rod at  $z^* = 0.03$ , the mean solution is satisfactorily predicted, while slight variations are noted for the RMS values. This is probably due to the sensitivity of modeling the exact movement of the magnetic stirrer, mainly for the non-dominant directions, compared to the real case.

Similarly, a satisfactory agreement is noted on the vertical distribution where the profiles are presented in figure 29. In addition to the coherent profile shape, the mean  $\langle u_1^* \rangle_t$  values are very well predicted. Slight variations are recorded on the RMS values near the edge of the rod at  $r^* = 0.6$  for the same reason stated previously.

For the dominant velocity component, the radial profiles of  $\langle u_2^* \rangle_t$  and those of  $\text{RMS}\{u_2^*\}_t$  are considered in figure 30. Here, the LES profiles are generally very well superposed over

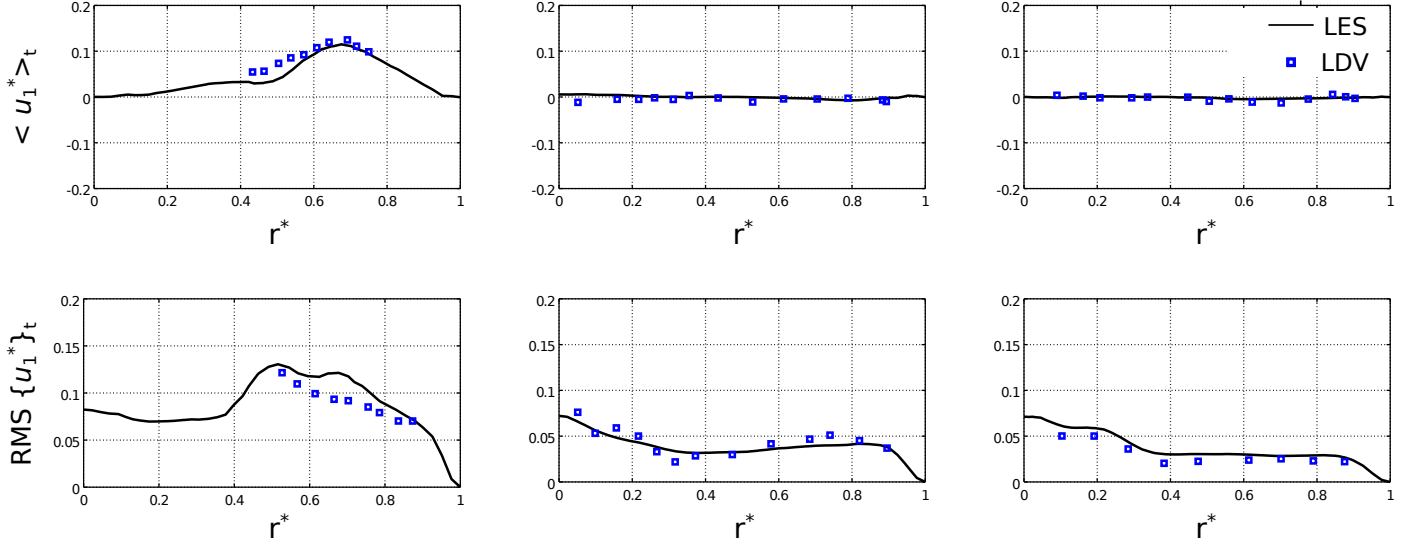


Figure 28: LES-LDV comparisons of the time-averaged radial velocity component  $\langle u_1^* \rangle_t$  (top) and its RMS  $\text{RMS}\{u_1^*\}_t$  (bottom) along three radial profiles at different heights. Left to right:  $z^* = 0.03, 0.28$  and  $0.47$  respectively.

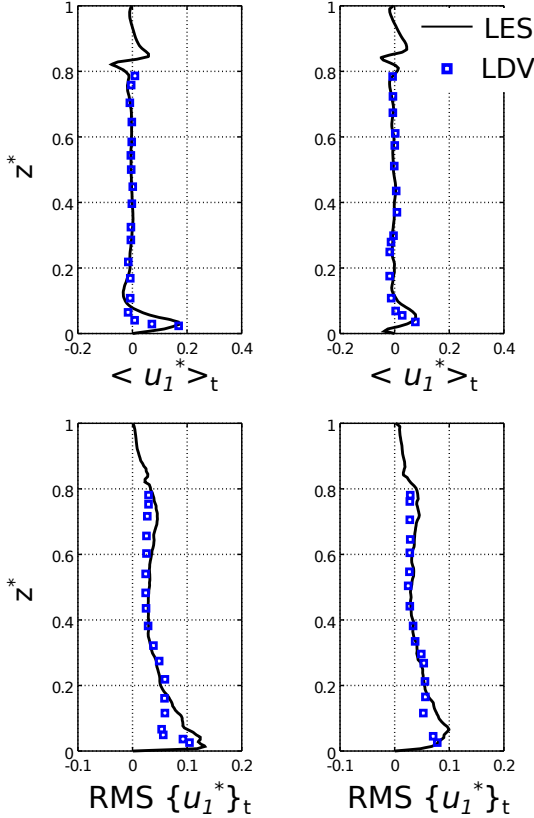


Figure 29: LES-LDV comparisons of the time-averaged radial velocity component  $\langle u_1^* \rangle_t$  (top) and its RMS  $\text{RMS}\{u_1^*\}_t$  (bottom) along two vertical profiles situated at  $r^* = 0.6$  (left) and  $r^* = 0.8$  (right).

the measured ones, except at the lowest profile near the edge of the rod ( $z^* = 0.1$  and  $r^* = 0.6 - 0.8$ ). At these local positions, the LES values overestimate the PIV by about 20%, which is also satisfactory. This justifies and confirms the convergence observed, both statistically and spatially.

The comparison regarding the third velocity component is finally considered in figures 31 and 32. Similarly, the profiles match very well in general, with slight variations that take place near the edge of the stirrer. As stated previously, the issue near the stirrer might be originating from the fact of modelling correctly the movement. More precisely, a no-slip boundary condition is prescribed at the rod without employing any wall function. Thus, the boundary layer that forms near the stirrer while rotating is not taken into account in the present version of IBM in TrioCFD. Another probable reason might be due to the statistical convergence of the RMS in that showed to be slow at this position. Accumulating more fields might lead to a better converged RMS fields and can reduce the recorded variations. However, in conclusion, it can be stated that the LES prediction is overall satisfactory and is very good away from the magnetic rod.

## 7. Concluding remarks

In this paper, results from an LES of a turbulent flow in a reactor with vortex effect are presented. The TrioCFD code with the discontinuous Front Tracking algorithm has been employed to perform the study. The first part of the work is devoted to the mesh sensitivity analysis where a second order convergence was obtained in accordance with the theory. A satisfactorily converged mesh has been identified so that the flow is not significantly influenced furthermore by a mesh refinement, at least regarding the time averaged quantities.

In the next part of the document, the flow pattern has been described, both instantaneously and statistically. The hydrodynamical activity taking place in the reactor, the formation of the two main vortices, in addition to the main oscillating zones have been well identified. This is a step for our future study in modelling the precipitation chemical reactions and the mixing phenomena that take place inside a reactor with vortex effect.

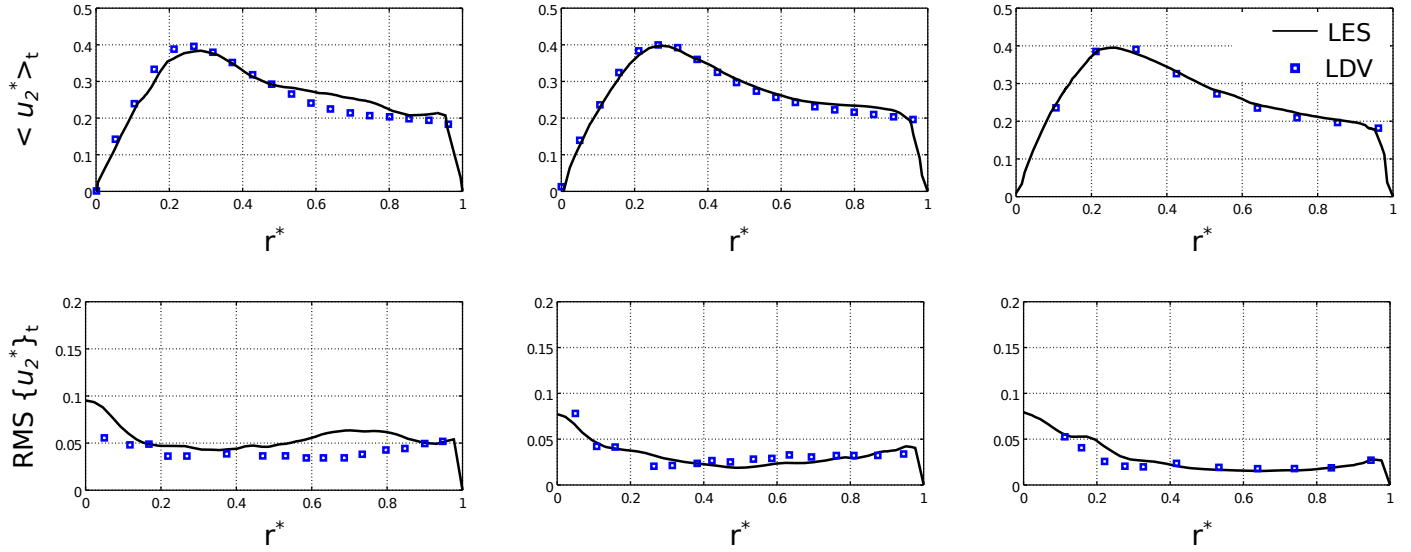


Figure 30: LES-LDV comparisons of the time-averaged tangential velocity component  $\langle u_2^* \rangle_t$  (top) and its RMS  $\{u_2^*\}_t$  (bottom) along three radial profiles at different heights. Left to right:  $z^* = 0.1, 0.28$  and  $0.47$  respectively.

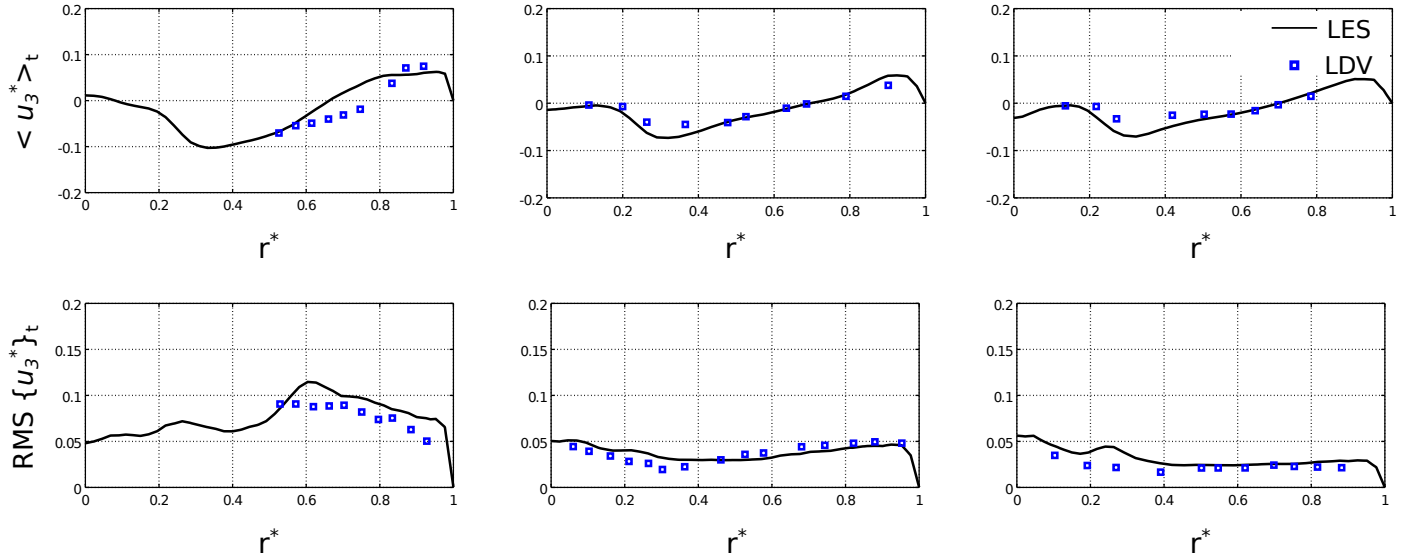


Figure 31: LES-LDV comparisons of the time-averaged axial velocity component  $\langle u_3^* \rangle_t$  (top) and its RMS  $\{u_3^*\}_t$  (bottom) along three radial profiles at different heights. Left to right:  $z^* = 0.03, 0.28$  and  $0.47$  respectively.

Analysis carried out on the statistical fields has shown a good convergence and a reasonable numerical error of the results.

Comparisons and validations of the LES data have been considered in the third and last part of this work. Theoretical models and experimental measurements from the literature have been employed to validate the length of the forced vortex critical radius and the shape/size of the vortex formed at the free-surface. Satisfactory agreement has been reported. Moreover, thanks to the available LDV measurements from the experimental work of CEA Grenoble that have served in validating the LES velocity predictions in the entire reactor. For both the time-averaged and the fluctuations fields, the agreement is satisfactory near the stirrer and very good far away.

For all these reasons and since to our knowledge no similar converged solutions have been reported in the literature, it can

be stated that this work serves as a reference LES data. Our future prospect is mainly the use of this converged hydrodynamic data to model the solid particles that form from precipitation in such types of reactors. A study on the effect of the stirrer rotating speed on the mixing phenomena is currently in progress.

### Acknowledgements

The authors would like to gratefully thank Christophe Bourcier for his help with the SALOME platform. This work was granted access to the HPC resources of CINES under the allocations A0052A07571 and A0062B07712 made by GENCI, attributed bonus hours used. We acknowledge the financial support of the Cross-Disciplinary Program on Numerical Simulation of CEA,

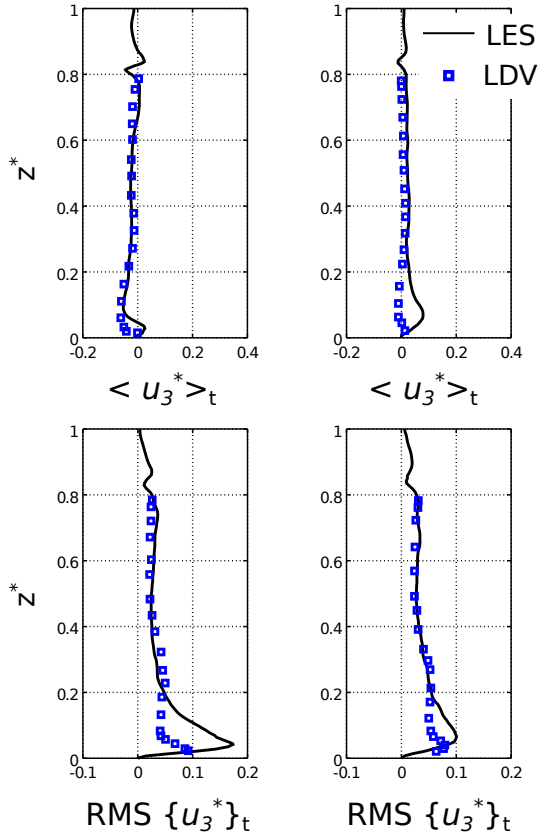


Figure 32: LES-LDV comparisons of the time-averaged axial velocity component  $\langle u_3^* \rangle_t$  (top) and its RMS  $\text{RMS}\{u_3^*\}_t$  (bottom) along two vertical profiles situated at  $r^* = 0.6$  (left) and  $r^* = 0.8$  (right).

the French Alternative Energies and Atomic Energy Commission.

## Nomenclature

$C_W$	WALE constant	[-]
$Re_s$	Stirring Reynolds number	[-]
$Fr$	Froude number	[-]
$N$	Number of independent samples	[-]
$t$	Time variable	[s]
$\delta t$	Time step	[s]
$\lambda_f$	Taylor time micro-scale	[s]
$H$	Height of the reactor	[m]
$H_i$	Height of the interface	[m]
$D$	Length of the magnetic rod	[m]
$d$	Diameter of the magnetic rod	[m]
$T$	Diameter of the reactor	[m]
$\Delta$	Characteristic cell size	[m]
$\Delta$	Maximum cell size	[m]
$\delta$	Minimum cell size	[m]
$\mathbf{x} = (r, \theta, z)$	Space vector	[m]
$r_c$	Critical radius of forced vortex	[m]
$\eta_{LES}$	Kolmogorov length scale	[m]

$\lambda_T$	Taylor length scale	[m]
$P$	Pressure	[Pa]
$V$	Volume of the reactor	[m <sup>3</sup> ]
$S$	Symmetrical strain tensor part	[s <sup>-1</sup> ]
$\Omega$	Rotational strain tensor part	[s <sup>-1</sup> ]
$N$	Frequency of the rod's rotation	[s <sup>-1</sup> ]
$f$	Frequency of the sampling	[s <sup>-1</sup> ]
$\mathbf{u} = (u_1, u_2, u_3)$	Velocity field	[m.s <sup>-1</sup> ]
$\sigma$	Surface tension	[N.m <sup>-1</sup> ]
$\rho_w$	Density of water	[kg.m <sup>-3</sup> ]
$\rho_a$	Density of air	[kg.m <sup>-3</sup> ]
$\dot{\theta}$	Angular velocity	[rad.s <sup>-1</sup> ]
$\nu_w$	Kinematic viscosity of water	[m <sup>2</sup> .s <sup>-1</sup> ]
$\nu_a$	Kinematic viscosity of air	[m <sup>2</sup> .s <sup>-1</sup> ]
$\nu_{SGS}$	Sub-Grid Scale viscosity	[m <sup>2</sup> .s <sup>-1</sup> ]
$\tau_{SGS}$	Sub-Grid Scale stress tensor	[m <sup>2</sup> .s <sup>-2</sup> ]
$\mathcal{K}^t$	Turbulent kinetic energy	[m <sup>2</sup> .s <sup>-2</sup> ]
$\epsilon_{LES}$	Total dissipation rate	[m <sup>2</sup> .s <sup>-3</sup> ]

## References

- [1] C Xuereb, M Poux, and J Bertrand. *Agitation et mélange: Aspects fondamentaux et applications industrielles*. Dunod, 2006.
- [2] M Yianneskis, Z Popielek, and JH Whitelaw. An experimental study of the steady and unsteady flow characteristics of stirred reactors. *Journal of Fluid Mechanics*, 175:537–555, 1987.
- [3] BN Murthy and JB Joshi. Assessment of standard k- $\epsilon$ , rsm and les turbulence models in a baffled stirred vessel agitated by various impeller designs. *Chemical engineering science*, 63(22):5468–5495, 2008.
- [4] A Brucato, M Ciofalo, F Grisafi, and G Micale. Numerical prediction of flow fields in baffled stirred vessels: a comparison of alternative modelling approaches. *Chemical Engineering Science*, 53(21):3653–3684, 1998.
- [5] P Auchapt and A Ferlay. Appareil à effet vortex pour la fabrication d'un procédé, 1981. Brevet FR 1 556 996.
- [6] S Nagata, N Yoshioka, and T Yokoyama. Studies on the power requirement of mixing impellers. *Memoirs of the Faculty of Engineering, Kyoto University*, 17:175–185, 1955.
- [7] DB Giaiotti and F Stel. The rankine vortex model. *University of Trieste - International Centre for Theoretical Physics*, 2006.
- [8] N Lamarque, B Zoppé, O Lebaigue, Y Dolias, M Bertrand, and F Ducros. Large-eddy simulation of the turbulent free-surface flow in an unbaffled stirred tank reactor. *Chemical Engineering Science*, 65(15):4307–4322, 2010.
- [9] PM Armenante, C Luo, CC Chou, I Fort, and J Medek. Velocity profiles in a closed, unbaffled vessel: comparison between experimental ldv data and numerical cfd predictions. *Chemical Engineering Science*, 52(20):3483–3492, 1997.
- [10] M Ciofalo, A Brucato, F Grisafi, and N Torracca. Turbulent flow in closed and free-surface unbaffled tanks stirred by radial impellers. *Chemical Engineering Science*, 51(14):3557–3573, 1996.
- [11] A Delafosse, A Line, J Morchain, and P Guiraud. Les and urans simulations of hydrodynamics in mixing tank: comparison to piv experiments. *Chemical Engineering Research and Design*, 86(12):1322–1330, 2008.
- [12] HS Yoon, S Balachandar, and MY Ha. Large eddy simulation of flow in an unbaffled stirred tank for different reynolds numbers. *Physics of fluids*, 21(8):085102, 2009.
- [13] SB Pope. *Turbulent flows*, 2001.
- [14] M Bertrand, E Plasari, O Lebaigue, P Baron, N Lamarque, and F Ducros. Hybrid les-multizonal modelling of the uranium oxalate precipitation. *Chemical engineering science*, 77:95–104, 2012.
- [15] JH Perry. *Chemical engineers' handbook*, 1950.

- [16] E Labourasse, D Lacanette, A Toutant, P Lubin, S Vincent, O Lebaigue, JP Caltagirone, and P Sagaut. Towards large eddy simulation of isothermal two-phase flows: Governing equations and a priori tests. *International journal of multiphase flow*, 33(1):1–39, 2007.
- [17] A du Cluzeau, G Bois, and A Toutant. Analysis and modelling of reynolds stresses in turbulent bubbly up-flows from direct numerical simulations. *Journal of Fluid Mechanics*, 866:132–168, 2019.
- [18] F Nicoud and F Ducros. Subgrid-scale stress modelling based on the square of the velocity gradient tensor. *Flow, turbulence and Combustion*, 62(3):183–200, 1999.
- [19] J Smagorinsky. General circulation experiments with the primitive equations: I. the basic experiment. *Monthly weather review*, 91(3):99–164, 1963.
- [20] PE Angeli, U Bieder, and G Fauchet. Overview of the trio cfd code: main features, v&v procedures and typical applications to nuclear engineering.
- [21] DEN-CEA. TrioCFD, <http://trioefd.cea.fr/>.
- [22] B Mathieu. A 3d parallel implementation of the front-tracking method for two-phase flows and moving bodies. *177ème Session du comité scientifique et technique de la Société Hydrotechnique de France, Advances in the modelling methodologies of two-phase flows, Lyon, France, 2004*.
- [23] A du Cluzeau, G Bois, A Toutant, and J-M Martinez. On bubble forces in turbulent channel flows from direct numerical simulations. *Journal of Fluid Mechanics*, 882, 2020.
- [24] EA Fadlun, R Verzicco, Paolo Orlandi, and J Mohd-Yusof. Combined immersed-boundary finite-difference methods for three-dimensional complex flow simulations. *Journal of computational physics*, 161(1):35–60, 2000.
- [25] M Belliard, M Chandesris, J Dumas, Y Gorsse, D Jamet, C Josserand, and B Mathieu. An analysis and an affordable regularization technique for the spurious force oscillations in the context of direct-forcing immersed boundary methods. *Computers & Mathematics with applications*, 71(5):1089–1113, 2016.
- [26] T Fortin. *Une méthode d'éléments finis à décomposition L2 d'ordre élevé motivée par la simulation des écoulements diphasiques bas Mach*. PhD thesis, Université Paris 6, 2006.
- [27] SALOME platform V9.4.0. <https://www.salome-platform.org/news>.
- [28] OCCIGEN-CINES. <https://www.cines.fr/calcul/materiels/occigen>.
- [29] E Saikali, G Bernard-Michel, A Sergent, C Tenaud, and R Salem. Highly resolved large eddy simulations of a binary mixture flow in a cavity with two vents: Influence of the computational domain. *International Journal of Hydrogen Energy*, 44(17):8856–8873, 2019.
- [30] E Saikali. *Numerical modelling of an air-helium buoyant jet in a two vented enclosure*. PhD thesis, Sorbonne Université, 2018.
- [31] DG Altman and JM Bland. Standard deviations and standard errors. *Bmj*, 331(7521):903, 2005.
- [32] JH McDonald. *Handbook of biological statistics*, volume 2. 2009.
- [33] GC Tiao, GC Reinsel, D Xu, JH Pedrick, X Zhu, AJ Miller, JJ DeLuisi, CL Mateer, and DJ Wuebbles. Effects of autocorrelation and temporal sampling schemes on estimates of trend and spatial correlation. *Journal of Geophysical Research: Atmospheres*, 95(D12):20507–20517, 1990.
- [34] A Le Lan and H Angelino. Etude du vortex dans les cuves agitées. *Chemical Engineering Science*, 27(11):1969–1978, 1972.